Comparison of Muscle Function Predictions Using Mass-enhanced and Massless Hill-type Muscle Models in Human Locomotion

by

Ing-Jeng (Evan) Chen

M.D., National Taiwan University, 2014

Thesis Submitted in Partial Fulfillment of the
Requirements for the Degree of
Master of Science

in the
Department of Biomedical Physiology and Kinesiology
Faculty of Science

SIMON FRASER UNIVERSITY
Spring 2024

Declaration of Committee

Name:	**Ing-Jeng (Evan) Chen**
Degree:	**Master of Science**
Title:	**Comparison of Muscle Function Predictions Using Mass-enhanced and Massless Hill-type Muscle Models in Human Locomotion**
Committee:	**Chair: Matthew White** Associate Professor, Biomedical Physiology and Kinesiology
	James Wakeling Supervisor Professor, Biomedical Physiology and Kinesiology
	Nilima Nigam Committee Member Professor, Mathematics
	Sabrina Lee Committee Member Lecturer, Biomedical Physiology and Kinesiology
	Dylan Cooke Examiner Assistant professor, Biomedical Physiology and Kinesiology

Ethics Statement

The author, whose name appears on the title page of this work, has obtained, for the research described in this work, either:

a. human research ethics approval from the Simon Fraser University Office of Research Ethics

or

b. advance approval of the animal care protocol from the University Animal Care Committee of Simon Fraser University

or has conducted the research

c. as a co-investigator, collaborator, or research assistant in a research project approved in advance.

A copy of the approval letter has been filed with the Theses Office of the University Library at the time of submission of this thesis or project.

The original application for approval and letter of approval are filed with the relevant offices. Inquiries may be directed to those authorities.

Simon Fraser University Library
Burnaby, British Columbia, Canada

Update Spring 2016

Abstract

Muscle mass significantly shapes skeletal muscle behavior and might partially clarify why traditional massless Hill-type models struggle to predict larger muscle functions in dynamic, submaximal contractions. However, the applicability of mass-enhanced Hill-type models in human locomotion remains unexplored. In my thesis, I compared predictions of human muscle performance (force, work output) between mass-enhanced and massless Hill-type models across varied scaled muscle sizes, tasks, and locomotion conditions. I observed minor but noteworthy mass effects in human-sized muscles across different tasks and muscles, escalating with scaled muscle mass. These effects were more pronounced at higher cycling cadences, unaffected by crank loads. Additionally, increased muscle mass resulted in a reduction in muscle mechanical work per cycle.

Keywords: skeletal muscle, muscle mechanics, muscle mass, inertia, cyclic contractions

Acknowledgements

I would like to first give a big shout-out to my supervisor, James Wakeling. From building experimental devices, conducting subject testing, step-by-step coding, data analysis, to thesis writing, you've been a guiding star in the wild world of muscle biomechanics. I couldn't be luckier to have a mentor like you.

I'd also like to give a huge thanks to Stephanie Ross, the brain behind the Muscle Mass project, for paving the way with your outstanding research contributions and for providing invaluable feedback and ideas during my research journey.

I am deeply grateful to my committee members, Nilima Nigam and Sabrina Lee, for pulling issues out of my brain and making science sounds like the coolest thing ever. Your active participation in discussions, particularly the debates with James, are like a shot of inspiration.

Big thanks to Evie Vereecke for being the trouble-shooting superhero during the pilot test. The box you crafted for the study more than a box; it's a container of memories and gratitude.

Finally, a heartfelt thank you to my partner in crime, my wife Tzu-Hui (Winnie). You've been the backbone, supporting my studies, taking care of kids, and sharing the ups and downs of life in a whole new country. Without you, the dream of Canadian adventures wouldn't have come true. Cheers to us!

Table of Contents

List of Tables

List of Figures

Chapter 1.

Effects of muscle mass on muscle function

1.1. The significance of studying skeletal muscle function

Skeletal muscle, the largest organ in the human body constituting approximately 40 % of an individual's body mass (Frontera & Ochala, 2015; Janssen et al., 2000), serves as the primary contributor to body movement and is also a crucial energy consumer (Zurlo et al., 1990). Identifying what factors can affect individual muscle function during movement and understanding how these factors contribute to force production offer valuable insights into human locomotion. In cases of abnormal movement patterns, this understanding can be employed to identify specific muscles that may not be functioning properly (Hicks et al., 2008; Steele et al., 2010), leading to the development of enhanced movement strategies or treatments (Gomes et al., 2017; Piazza, 2006) and influencing the design of various assistive devices (Uchida et al., 2016; Grimmer & Seyfarth, 2014; Federici et al., 2015).

1.2. Why use muscle models to study muscle function?

Compared to external force, which results from the interaction between human body and its environment and can be quantified using a force measuring instrument, directly measuring the internal force generated by a muscle poses challenges. One method involves using a tendon buckle to directly measure the tendon strain induced by external forces applied to the tendon (Loeb et al., 1985; Walmsley et al., 1978). Assuming that the external forces are transmitted in series from the internal muscle force, muscle force could be estimated by this method. However, in cases where multiple muscles contribute forces to a conjoint tendon, it becomes challenging to measure individual muscle forces using this method. Additionally, this direct measuring approach is highly invasive, requiring a surgical procedure to secure the tendon buckle on the tendon, making it impractical and ethically unsound for application in live human subjects during movement. Another method for estimating muscle force involves using a dynamometer to measure external forces or moments produced by muscles (Andrews, et al., 1996). However, as most of our joints are crossed by more than one muscle, dynamometer-

measured forces and moments are influenced by all muscles crossing the joint. Therefore, it is not possible to measure individual muscle force using this method. Our current comprehension of human muscle function during locomotion is often extrapolated from non-human animal experiments, assuming that muscle properties are conserved across vertebrates. Alternatively, non-invasive measures such as muscle activity through surface electromyography (EMG) (Blake & Wakeling, 2014, 2015), muscle shape changes via ultrasound (Cronin & Lichtwark, 2013; Van Hooren et al., 2020), or magnetic resonance imaging (MRI) (Asakawa et al., 2003) allow indirect inference of the mechanical behaviours of human muscles. These measures can also serve as inputs for computational muscle models to predict *in vivo* muscle forces during dynamic contractions. Such models have significantly expanded our understanding by simulating experiments that are challenging or impossible to conduct on real muscles. Moreover, they can be applied across diverse species, various movement activities, and different hypothetical scenarios.

1.3. Traditional Hill-type muscle models and their limitations

Traditional one-dimensional (1D) Hill-type muscle models are the most widely-used muscle models in biomechanics, serving as the representation of muscle actuators in musculoskeletal models. These models typically consist of a contractile element (CE), a parallel elastic element (PEE), and a series elastic element (SEE), The CE is related to muscle fibres generating forces through the cross-bridges forming between the actin and myosin filaments. Simultaneously, the PEE comprises the passive component of the sarcomere, contributing to muscle stiffness and resisting stretching. The SEE involves the passive contributions of the tendon and aponeurosis, transmitting the force generated by the CE to the tendon (Zajac, 1989). These models offer estimates of muscle forces based on the muscle activation state and assumed force-length and force-velocity relationships. They require minimal muscle-specific parameters, and consequently have the strength of low computational costs and relative operational simplicity.

However, since Hill-type muscle models offer a simplified representation of the complex physiological mechanisms of muscle contraction, some limitations need to be considered. For example, the intrinsic properties of these models are derived from experiments on single fibres or small fibre bundles that are fully activated and constrained to maintain a steady-state contraction (Zajac, 1989; Thelen, 2003). Consequently, the

accuracy of muscle force predictions by Hill-type models is likely compromised during submaximal, dynamic muscle contractions in daily functional activities like walking, where muscle activations, lengths, and velocities vary. Research by Millard and his colleagues (2013) showed that muscle forces reproduced by Hill-type musculotendon models exhibit fewer errors under maximally-activated conditions than under submaximally-activated conditions. Perreault and colleagues (2003) found that the root-mean-squared errors between measured and modeled forces in cat soleus muscle were higher than 50 % during natural normal locomotion, characterized by large muscle excursions and submaximal muscle activation. Similarly, increased modelling errors were observed in goats and humans during *in vivo* locomotion (Lee et al., 2013b; Dick et al., 2017). Moreover, Hill-type models overlook several factors that could impact the predictive accuracy of muscle function, including the effects of different muscle fibre types (Wakeling et al., 2012), history-dependent effects (Abbott & Aubert, 1952; Herzog & Leonard, 2000, 2002), muscle mass effects (Günther et al., 2012; Ross & Wakeling, 2016, 2021; Ross et al., 2020), and three-dimensional (3D) effects (Rahemi et al., 2014; Ross et al., 2018, 2021). For example, many Hill-type models assume a homogenous fibre type within the muscle, despite muscles being broadly classified into fast and slow fibre types, which have different activation-deactivation pattern depending on the motor tasks (Lee et al., 2013a; Wakeling, 2004) and may be excited independently or together. Lee and colleagues (2013b) demonstrated that a Hill-type model incorporating both fast and slow contractile elements can enhance muscle force prediction in goats during locomotion tasks, resulting in up to a 37.4 % reduction in root-mean-squared errors compared to a single-element model.

1.4. The effects of muscle mass

The effects of muscle mass have only received attention in recent years. In traditional Hill-type muscle models, muscles were assumed to be massless, and the behaviour of the entire muscle was assumed to mimic that of a single muscle fibre. This assumption came into question when Josephson and Edman (1988) found that the maximum shortening speed of faster fibres within a fibre bundle was lower than that of single fibres taken from the same bundle. They suggested that the load from adjacent fibres might slow the contraction speed of fibres in the whole muscle. Additionally, Holt and colleagues (2014) found that when fibres within muscle are not fully activated, even if the active fibres are entirely fast fibres, the muscles contract more slowly compared to

when all the fibres within the muscle are fully activated. The study proposed that inactive fibres contribute inertial resistance to the contraction of active fibres rather than contributing force. However, mass effects were only proposed as a potential explanation and had not been tested in experiments until Günther and his colleagues (2012) developed a model incorporating muscle mass effects. This first *in silico* study found that the internal mass slows the rate of force development, possibly due to the time it takes for mass within muscle tissue to move in response to force-generated accelerations (Günther et al., 2012). Further *in silico* simulation experiments using a mass-enhanced Hill-type model demonstrated that increasing muscle mass reduces the maximum contraction speeds (Ross and Wakeling, 2016). It also decreases the mass-specific mechanical work output per cycle of muscles during both simulated (Ross et al., 2018a) and *in situ* (Ross et al., 2020; Ross & Wakeling, 2021) cyclic contractions, especially for muscles with a fast fibre type (Ross & Wakeling, 2021). The efficiency of muscle contraction is also diminished with increased muscle mass (Ross & Wakeling, 2021). Moreover, three-dimensional models that account for muscle mass highlight that greater muscle mass leads to heightened mass-specific internal kinetic energy, increased energy stored in the aponeurosis, and non-uniform tissue acceleration during contractions (Ross et al., 2021).

If the muscle mass effect is considered negligible, and a larger muscle is assumed to behave similarly to a small muscle fibre, geometrically scaling up the length of a muscle to n times its original length would theoretically result in its maximum generated force increasing n^2 times, as the force is proportional to the physiological cross-sectional area of the muscle. However, it has been observed that prediction errors between modeled and measured forces increase with growing muscle mass, faster contraction speeds, and decreasing levels of muscle activation (S. S. Lee et al., 2013; Dick et al., 2017; Ross et al., 2020; Wakeling et al., 2021). This discrepancy is explained by the fact that the muscle's volume, assuming constant density, increases n^3 times larger with the lengthening of the muscle, leading to a greater internal load relative to the force it can produce to accelerate its internal mass (Ross and Wakeling, 2016). Consequently, the larger the scale-up value, the higher the relative inertial cost of contraction. Furthermore, because inertial resistance is not solely associated with the magnitude of mass but also with acceleration, mass effects are likely more pronounced during cyclic movements with high frequency or significant changes in muscle length, where the acceleration of the mass is higher.

In summary, inertial resistance due to muscle mass can diminish the muscle's rate of force development, maximum contraction speed, work output per cycle, and overall efficiency of muscle contraction. This effect is more pronounced in larger muscle sizes, during high-frequency or high-strain cyclic movements, and during submaximal contractions. Therefore, it may be crucial to consider this effect for enhancing the predictive accuracy of muscle models.

1.5. The mass-enhanced Hill-type muscle model

To understand the interaction between muscle internal mass and muscle contraction dynamics, Günther and colleagues (2012) developed a muscle model comprising a finite number of Hill-type contractile elements and point masses evenly distributed throughout the muscle mass. This model simulated accelerated contractions involving alternating sequences of the contractile elements and point masses in a fully active state. Building upon this, Ross and Wakeling (2016; 2018a) modified the mass-enhanced model to investigate the impact of muscle mass on function during submaximal and cyclic contractions. More recently, Ross and co-workers (2020) conducted a living rat experiment, manipulating the effective mass of the plantaris muscle to examine the effects of increased muscle mass on mechanical work during cycling contractions. They also simulated the experimental muscle contractions with the mass-enhanced Hill-type muscle model for validating the results of previous modelling work. However, this model has only been tested in *in silico* and *in situ* studies and has not been applied to large muscles in living humans during submaximal cyclic movements, where muscle mass might have the most significant effect. Therefore, several questions remain unanswered: (i) It is unknown whether human muscle performance (e.g., muscle forces, power output, work output) during locomotion, as predicted by the mass-enhanced model, significantly differs from predictions made by the traditional massless model. (ii) How the predicted forces and the differences in predicted forces between the two models change with muscle size and the cadence of cyclic movement is yet to be determined.

1.6. Aims

In this thesis, my goal was to employ a mass-enhanced Hill-type model for simulating experimental contractions of human muscles during activities such as walking

and cycling. I conducted a comparative analysis of the predicted muscle performances using both mass-enhanced and massless Hill-type muscle models. This comparison was conducted across various scaled muscle sizes, different muscles of the lower extremities, and diverse movement tasks and conditions. In Chapter 2, I collected kinematic, kinetic, and electromyographic (EMG) data from the lower limb muscles of 20 healthy participants, examining the mass effects on model-predicted forces during various daily activities such as walking, running, sit-to-stand, and hopping. I hypothesized that: (1) there would be a significant difference between the normalized muscle forces predicted by the mass-enhanced model and those predicted by the massless model. (2) As the muscle size was scaled up, the difference between the two model-predicted forces would become more pronounced, indicating greater mass effects in larger-sized muscles. In Chapter 3, I conducted simulations of experimental contractions in human muscles under different cycling conditions. I hypothesized that (1) Mass effects would be more prominent during cycling compared to daily activities. (2) Higher cadences of cyclic movement could result in greater mass effects, while crank load did not influence mass effects.

Chapter 2.

Effects of muscle mass on muscle force predictions in human daily activities

2.1. Abstract

Mass effects have emerged as a significant factor influencing muscle performance. In response to this, a dynamic, multi-segment Hill-type model (mass-enhanced model), incorporating mass effects, has been developed to address the inaccuracies inherent in traditional massless models. However, its application to human muscles undergoing submaximal, dynamic contraction during locomotion remains untested, leaving the significance of mass effects on human muscle performance unknown. This study aimed to compare muscle forces predicted by mass-enhanced and massless models, assessing the extent of mass effects on human muscle performance during locomotion. Twenty participants were recruited for collecting kinematic, kinetic, and electromyographic (EMG) data during walk, running, hopping, and sit-to-stand tasks. Mass-enhanced and massless Hill-type models were driven to simulate experimental muscle contraction. The primary outcomes included the root-mean-squared errors (RMSE) and coefficient of determination (r^2) in predicted muscle forces between these models, compared across different scaled muscle sizes and movement tasks. Higher RMSE value indicates greater mass effects. Our results indicated that muscles scaled to 10^3 times their original mass consistently exhibited larger RMSE and lower r^2 compared to muscles with original or 10^{-3} smaller scaled size across all tested muscles and movement tasks (P<0.001). The highest recorded RMSE was 7.228±0.181 % $\hat{F}_0$ for VL in running. Although RMSE values were minor in original or smaller-sized muscles, significant differences persisted in log-transformed RMSE values between muscles with original and 10^{-3} times smaller sizes. Furthermore, RMSE were larger in running and hopping compared to walking and sit-to-stand tasks for all muscles tested, potentially attributed to the higher acceleration of muscle mass. In conclusion, while mass effects can significantly influence muscle performance during human locomotion, their impact is minimal in human-sized or smaller muscles during slower activities. However, they become more prominent at larger scaled sizes and are intensified by the movement's cadence.

2.2. Introduction

Traditional one-dimensional (1D) Hill-type muscle models, the most widely-used models representing muscle actuators, have broadened our knowledge by simulating experiments that either have not been conducted on real muscles or are impractical due to invasiveness on living human muscles (Loeb et al., 1985; Walmsley et al., 1978). These models for musculoskeletal simulations find applications across various domains including different species (Full & Ahn, 1995; Kargo et al., 2002; Lee et al., 2013), movement activities (Delp et al., 2007; Dick et al., 2017; Lai et al., 2019), and hypothetical scenarios (Ross et al., 2018b; Hutchinson & Garcia, 2002). Moreover, they hold clinical potential for analyzing kinetic or kinematic changes in neuromuscular disorders (Hicks et al., 2008; Steele et al., 2010), developing rehabilitation strategies (Hall et al., 2011; Peterson et al., 2011), and influencing the design of assistive devices (Uchida et al., 2016). They provide estimates of muscle forces which are related to the muscle activation state, and the intrinsic force-length and force-velocity properties of muscle fibres, with minimal requirements for muscle-specific parameters (Hill, 1938; Kaufman et al., 1991; Wakeling et al., 2012; Dick et al., 2017), and thus have the strength of low computational cost and being relatively simple to operate. However, the intrinsic properties of the traditional Hill-type models are typically determined by experiments on fully-activated single fibres, fibre bundles, or small muscles during steady contractions, where muscle mass is minimal and muscle acceleration is absent. When extrapolating these models to predict forces generated by larger muscles, it is assumed that the entire muscles behave similarly to geometrically scaled versions of these individual fibres or bundles (Zajac, 1989; Thelen, 2003; Millard et al., 2013). This implies that forces scale proportionally to the muscle's cross-sectional area, while lengths and velocities scale in proportion the muscle's length. Nonetheless, when comparing these models' predictions with experimental measurements of entire muscle, the accuracy of traditional Hill-type models diminishes, especially in conditions deviating from the fully-activated, steady-state contractions used in single fibre or small muscle experiments (Perreault et al., 2003; Dick et al., 2017; Wakeling et al. 2021). While the discrepancies between model predictions and experimental measures may be influenced by factors such as fibre-type composition and recruitment patterns (Wakeling et al., 2012; Dick et al., 2017), muscle geometry and architecture (Hodgson et al., 2006; Azizi et al., 2008), and tissue properties in whole muscle (Pappas et al., 2002; Soman et al., 2005; Shin et al., 2009), they can also be

attributed to the assumption that larger or whole muscles behave similarly to larger-scaled single fibres. These “massless” models might fail to account for the complexities of larger muscle dynamics because they overlook the force and power required to accelerate the tissue mass.

While tissue mass might have a negligible impact on the behaviours of single fibres or small muscles, its effect may increase notably in larger muscles. When factoring in muscle mass within a force system during contraction, the inertial resistance due to the mass opposes changes in motion or rest. Activated sarcomeres must produce force to surpass this inertial resistance, accelerating their own or neighboring masses within the muscle. In terms of energy utilization, as a muscle operates with a finite amount of energy during contraction, energy required to accelerate internal mass becomes unavailable for the muscle to perform external work (Wakeling et al. 2020; Ross & Wakeling, 2021). As a result, this interplay between the inertial resistance due to the mass and the usage of the force or energy within the muscle could affect the external force and work output of the muscle. As muscles increase in size with identical geometric properties, their force-generating capacity scales with their cross-sectional area, while their mass scales with their volume. Consequently, larger muscles experience higher inertial loads compared to the force they can generate. This disparity becomes more pronounced during submaximal contraction because the force is less. Moreover, since inertial force depends on both mass and its acceleration, its effect is likely most significant not only when a muscle has substantial mass and undergoes submaximal contractions but also in unsteady contractions with high cycle frequencies and rapid changes in velocity, where muscle acceleration is largest (Lee et al., 2013; Ross & Wakeling, 2016; Dick et al., 2017; Ross et al., 2020; Wakeling et al., 2021).

The effect of muscle mass has not been in the scope of studies on muscle function until recent years. Josephson and Edman (1988) found that the maximum shortening speed of faster fibres within a fibre bundle were lower than that of single fibres taken from the same bundle, and suggested that the load from adjacent fibres might slow the contraction speed of fibres in whole muscle. Additionally, when fibres within muscle are not fully activated, the inactive fibres are considered to provide inertial resistance to active fibre contraction instead of contributing force, thus slowing muscle contraction (Holt et al., 2014). To understand how muscle internal mass interacts with muscle contraction dynamics, a “mass-enhanced” Hill-type muscle model was proposed by Günther and

colleagues (2012). The model consisted of a finite number of Hill-type models placed in-series with the muscle mass evenly distributed as point masses. In their study, they discovered that the presence of internal mass within muscle tissue impeded the rate of force development because the mass required time to move in response to force-generated accelerations. More recently, simulation studies with mass-enhanced models have shown that the mass effect hinders the maximum shortening speed of the entire muscle, (Ross & Wakeling, 2016), reduces the mechanical work output of muscles (Ross et al., 2018), and results in lower contraction efficiency for muscles that are primarily active during shortening (Ross & Wakeling, 2021). In an animal experiment it was also found that increasing effective internal mass and accelerations in a muscle reduces mechanical work output during cyclic contraction (Ross et al., 2020). Meanwhile, a mass-enhanced Hill-type model was validated by reproducing similar results to those observed in this experimental study (Ross et al., 2020). However, to date mass-enhanced models were only tested in *in silico* and *in situ* studies, but have not been used to simulate human movement. There have been no previous scientific studies investigating the effects of muscle mass in living human muscles during daily activities, in which muscles undergo submaximal contraction and cyclic movement, and tissue inertia likely has large effect. Therefore, there are some questions remaining open. (i) Whether a mass-enhanced model can be run to simulate experimental muscle contractions in living human during movement of daily activities. (ii) Whether muscle mass has an effect on the mechanical output of human muscle during daily activities, and how the extent of this mass effect changes with muscle size.

To address these questions, we used a mass-enhanced Hill-type model to simulate experimentally measured contractions of human muscles during daily activities such as walking and sit-to-stand. We scaled experimental kinematic inputs and muscle geometric data (length, cross-sectional area, volume, thereby affecting mass) to different sizes to examine the effect of muscle mass on the model's predictions of muscle forces and how the effect changes with different scaling sizes. These performance outputs obtained from the mass-enhanced model were then compared with those from a traditional massless Hill-type model across various lower-limb muscles and different movement tasks. Two hypotheses were tested: (H1) a notable discrepancy would exist in predicted muscle forces between the two models, and (H2) this discrepancy would intensify as the muscle

size increased, correlating with heightened inertial resistance attributed to greater muscle mass.

2.3. Methods

2.3.1. Acquisition of Experimental Data

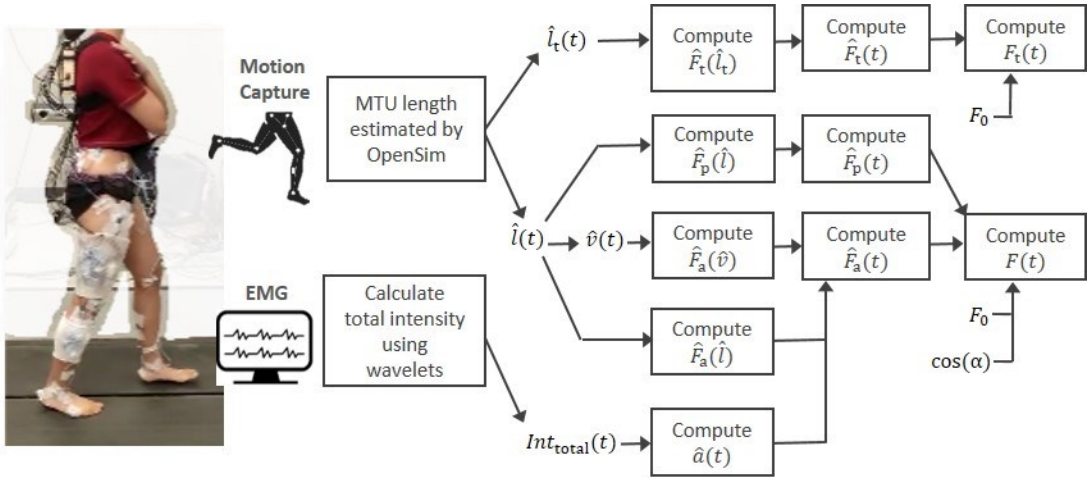

Figure 2.1. Diagrammatic depiction of data collection and processing.
A comprehensive set of kinematic, kinetic, and electromyographic (EMG) data of right lower limb during movement was collected using motion capture system, force plates, and EMG. The time-varying muscle-tendon unit (MTU) length and total intensity of EMG ($Int_{\text{total}}(t)$) were estimated using OpenSim and wavelet functions, respectively, and then were used to calculate time-varying normalized muscle fibre length ($\hat{l}(t)$), tendon length ($\hat{l}_t(t)$), and muscle activation level ($\hat{a}(t)$), as inputs to drive Hill-type muscle models for predicting time-varying muscle force ($F(t)$) and tendon force ($F_{\text{t}}(t)$). $l(t)$: muscle fibre length; $l_{\text{t}}(t)$: tendon length; $\hat{v}(t)$: normalized muscle contraction velocity; $\hat{F}_{\text{a}}(t)$: normalized active muscle force; $\hat{F}_{\text{p}}(t)$: normalized passive muscle force; α: muscle pennation angle; F_0: maximum muscle fibre force; $\hat{F}_{\text{t}}(t)$: normalized tendon force.

We recruited participants from local communities surrounding Simon Fraser University, and all participants gave informed consent. The study protocols were approved by the Institutional Ethics Review Boards at Simon Fraser University. Ultimately, twenty adult participants (10 females; age (mean±s.d.): 33±10.7 years old; weight: 66.3±10.1 kg; height: 1.7±0.1 m) were tested for collecting comprehensive sets of kinematic, kinetic, and electromyographic (EMG) data (Figure 2.1). For each participant, 24 LED motion-capture markers were secured bilaterally on the skin over the pelvis and lower extremities, as described in a previous study (Dick et al., 2016). The 3D positions of these markers were sampled at 100 Hz using a dual-head optical motion capture system (Optotrak Certus, NDI, Waterloo, Canada). To record muscle electrical activity, bipolar Ag/AgCl surface

EMG electrodes (10 mm diameter, 21 mm spacing; Norotrode; Myotronics, Kent, USA) were positioned over the bellies of 10 muscles in the right lower extremity (Dick et al., 2016) after prior cleaning with alcohol and shaving to clean the skin. EMG signals were pre-amplified (gain 1000-5000), band-pass filtered (bandwidth 10–500 Hz; Biovision, Wehrheim, Germany), and sampled at 2000Hz. Ground reaction forces for both feet were recorded at 300 Hz using the dual force plates of an instrumented treadmill (Bertec FP6012-15; Ohio, USA).

Prior to the test session, a static calibration trial was conducted to scale the musculoskeletal model to each subject, based on distances between marker pairs. Maximal voluntary isometric contraction (MVC) trials were performed for the tested muscles: tiabialis anterior (TA), medial gastrocnemius (MG), lateral gastrocnemius (LG), soleus (SOL), rectus femoris (RF), vastus medialis (VM), vastus lateralis (VL), biceps femoris (BF), semitendinosus (ST), and Gluteus maximus (GM); the maximum excitation for each muscle recorded from these trials and the test session was used for EMG normalization. Subjects then continued with a five-minute warm-up by walking on the treadmill (to minimize the influence of temperature on the muscle excitations).

For the test session, participants were required to perform the following four tasks in order on the treadmill: walking and running at their preferred speed, hopping at a tempo of 110 beats per minute (BPM) timed to a metronome, and sit-to-stand from a chair at the tempo of 15 cycles per minute. All the data were collected for 30 s for each task. Then the tasks were repeated in reverse order after a 10-minute break.

Table 2.1. Model and equation parameters.

	Definition	**Value**	**Source**
σ_0	Maximum isometric muscle stress (Pa or N $\cdot$ m^{-2})	225000	Estimated, Medler, 2002
ρ	Muscle density (kg $\cdot$ m^{-3})	1060	Mendez & Keys, 1960
n	The number of muscle mass points	16	Ross et al., 2018b
v_0	Maximum unloaded muscle shortening velocity (s^{-1})	5 and 10 for slow and fast fibres, respectively	Wakeling et al., 2012
τ_{act}	Time constant for activation (s)	0.045 and 0.025 for slow and fast fibres	Dick et al., 2017
β	Ratio of τ_{act} to deactivation time constant	0.6	Dick et al., 2017

$R_{\mathrm{m-to-MTU}}$	Muscle-to-MTU length ratio		
	MG, medial gastrocnemius	0.54	Kovács et al., 2020
	SOL, soleus	0.60	
	VL, vastus lateralis	0.87	O'Brien et al., 2010
	RF, rectus femoris	0.73	
$l_{0,\mathrm{MTU}}$	Optimal MTU length (m)	Equation 2.2	Calculated
l_0	Optimal muscle length (m)	Equation 2.17 – 2.21	Calculated
$l_{\mathrm{t,slack}}$	Slack tendon length (m)	Equation 2.17 – 2.21	As above
$l_{\mathrm{MTU,initial}}$	Initial MTU length	Median value of MTU length data throughout a task	Obtained from experimental data
l_{initial}	Initial muscle length (m)	Equation 2.22 – 2.26	Calculated
$l_{\mathrm{t,initial}}$	Initial tendon length (m)	Equation 2.22 – 2.26	Calculated
V_{total}	Total muscle volume of one lower leg (m^3)	Equation 2.3	Handsfield et al., 2014
fr_{muscle}	MG, medial gastrocnemius	0.0362	Handsfield et al., 2014
	SOL, soleus	0.0621	
	VL, vastus lateralis	0.1166	
	RF, rectus femoris	0.0379	
V_{muscle}	Muscle volume (m^3)	Equation 2.4	Handsfield et al., 2014
$PCSA_0$	Muscle optimal physiological cross-sectional area (m^2)	Equation 2.5	Calculated
F_0	Maximum isometric muscle force (N)	Equation 2.6	Calculated

2.3.2. Experimental Data Processing

The EMG signals were quantified by their total intensity (a function of the square of EMG signals), which was calculated across a 10-450 Hz frequency band using an EMG-specific wavelet analysis (von Tscharner, 2000). The EMG intensity was normalized to the maximum intensity. Considering the linear relationship between muscle force and the amplitude of EMG signal (Milner-Brown & Stein, 1975), the square root of the normalized EMG intensity served as a measure of normalized muscle excitation ($\hat{u}(t)$). The normalized muscle excitation was converted to an activation level ($\hat{a}(t)$) using a transfer function (Zajac, 1989):

$$\frac{d\hat{a}(t)}{dt} + \frac{\hat{a}(t)}{\tau_{\mathrm{act}}} \cdot \left(\beta + \hat{u}(t) \cdot (1-\beta)\right) = \frac{\hat{u}(t)}{\tau_{\mathrm{act}}} \qquad (2.1)$$

where β= 0.6 and τ_{act}= 0.045. Details for this process have been described elsewhere (Lee et al., 2011; Dick et al. 2017).

The subject-specific LED maker positions were imported to a musculoskeletal simulation environment (OpenSim 4.3: Delp et al., 2007). A generic musculoskeletal model (Rajagopal et al., 2016) was scaled to generate a subject-specific model using data from the static trial of the participant. Subject-specific values of optimal fibre length, slack tendon length, and pennation angle were extracted from the musculoskeletal model. These values were used to calculate the subject-specific optimal MTU length ($l_{0,\mathrm{MTU}}$) as follows:

$$l_{0,\mathrm{MTU}} = l_{\mathrm{f,0,OpenSim}} \cdot \cos\left(\alpha_{\mathrm{OpenSim}}\right) + l_{\mathrm{t,slack,OpenSim}} \tag{2.2}$$

where $l_{\mathrm{f,0,OpenSim}}$ is optimal fibre length, $\alpha_{\mathrm{OpenSim}}$ is pennation angle, and $l_{\mathrm{t,slack,OpenSim}}$ is slack tendon length. Using the 'Inverse Kinematics tool', the time-varying muscle-tendon unit (MTU) length ($l_{\mathrm{MTU}}(t)$) during each task was estimated. Subsequently, $l_{\mathrm{MTU}}(t)$ was normalized to $l_{0,\mathrm{MTU}}$.

2.3.3. Muscle Models

A mass-enhanced Hill-type muscle model (Günther et al., 2012; Ross & Wakeling, 2016; Ross et al., 2018b) and a traditional Hill-type (massless) muscle model (Ross & Wakeling, 2016) were used to estimate the time-varying forces produced by the lower extremity muscles during the four different locomotor tasks.

We simplified the architecture of muscles and ignored the influence of multiple fibre types (Lee et al., 2011) to reduce the complexity of computation. The muscles were assumed to (1) have no aponeurosis or internal tendon, (2) have constant volumes depending on subject's mass and height (Handsfield et al., 2014), (3) have parallel fibres aligned with the contraction direction of the muscle, and thus having fibre length equivalent to the muscle belly length and a pennation angle of zero, (4) and have a fixed end and a free end that is connected to a serial elastic element (SEE) representing the tendon. Furthermore, the maximum isometric muscle stress (σ_0 = 225 kPa; estimated from literature of Medler, 2002), muscle density (ρ = 1060 kg m^{-3}; Mendez & Keys, 1960), and maximum unloaded muscle shortening velocity (v_0= 5 s^{-1}; Wakeling et al., 2012) were assumed constant. Total muscle volume of one lower leg (V_{total}; m^3) was given by:

$$V_{\mathrm{total}} = (47 \cdot W \cdot H + 1285) \cdot 10^{-6} \tag{2.3}$$

where W and H were participant's weight and height, respectively (Handsfield et al., 2014). The individual muscle volume (V_{muscle}) was calculated as:

$$V_{\mathrm{muscle}} = V_{\mathrm{total}} \cdot fr_{\mathrm{muscle}} \tag{2.4}$$

where fr_{muscle} was the fraction of individual muscle volume relative to V_{total}.The individual muscle mass was the product of V_{muscle} and ρ. The optimal physiological cross-sectional area ($PCSA_0$; m^2) was give by:

$$PCSA_0 = V_{\mathrm{muscle}} \cdot l_0^{-1} \tag{2.5}$$

where l_0 was optimal muscle length determined by Equation 2.17 – 2.21 . The maximum isometric muscle force (F_0; N) was calculated as:

$$F_0 = PCSA_0 \cdot \sigma_0 \tag{2.6}$$

Massless Hill-type muscle model

The massless Hill-type muscle model consisted of a contractile element (CE) and a parallel elastic element (PEE) (Figure 2.2). The muscle force generated by the CE was related to the muscle activation state ($\hat{a}(t)$), active force-length ($\hat{F}_{\mathrm{a}}(\hat{l})$) and active force-velocity ($\hat{F}_{\mathrm{a}}(\hat{v})$) relationships, whereas the PEE force depended on only the passive force-length relationship ($\hat{F}_{\mathrm{p}}(\hat{l})$). These relationships were modelled by employing Bézier curves (Ross et al., 2018) fitted to experimental data for CE forces (Winters et al., 2011) and PEE forces (Roots et al., 2007). The muscle force ($F(t)$) was calculated by the following equation (Roots et al., 2007):

$$F(t) = F_0 \cdot \left(\hat{a}(t)\hat{F}_{\mathrm{a}}(\hat{l})\hat{F}_{\mathrm{a}}(\hat{v}) + \hat{F}_{\mathrm{p}}(\hat{l})\right) \cdot \cos\alpha \tag{2.7}$$

where pennation angle (α) was 0 as fibres were assumed to be aligned with the contraction direction, and F_0 is the product of σ_0 and $PCSA_0$.

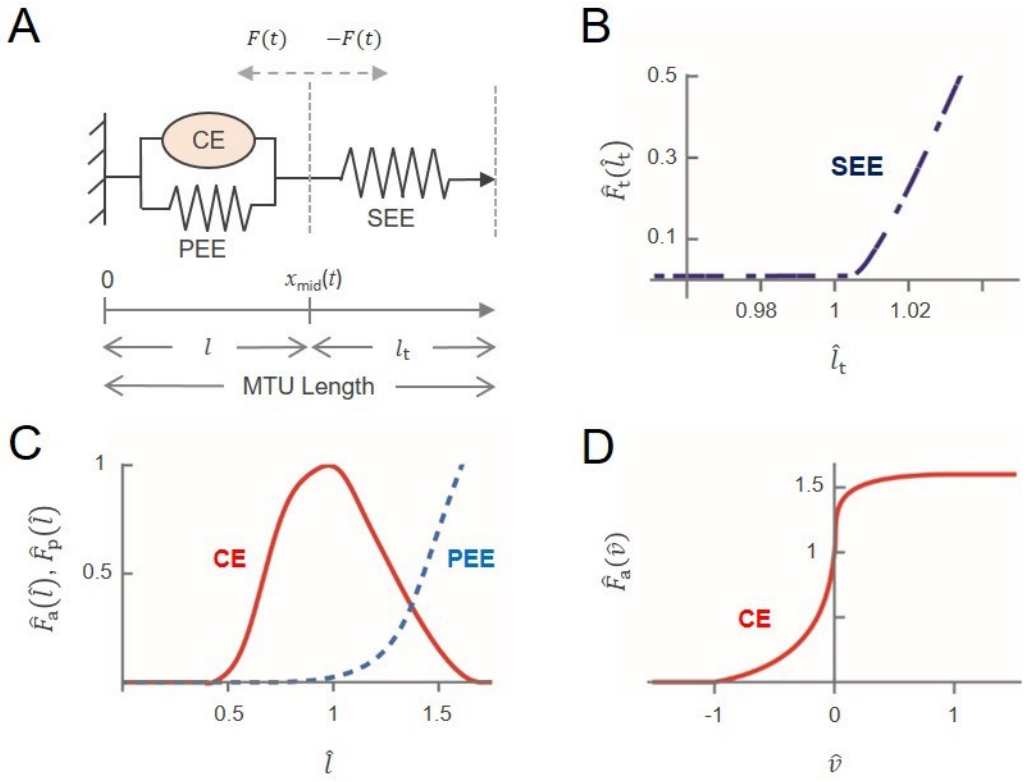

Figure 2.2. The massless Hill-type muscle model used to simulate experimental contraction cycles.

The model consisted of an active muscle component (CE, contractile element), a passive muscle component (PEE, parallel elastic element), and a tendon (SEE, serial elastic element) (A). The muscle force is the sum of forces from CE and PEE, depending on normalized activation level, normalized muscle force-length property (C), and normalized muscle force-velocity property (D). The tendon force from SEE depends on tendon force-length property (B). $X_{\mathrm{mid}}(t)$, the time-varying position of the muscle-tendon junction, which equaled to l, the muscle length; l_{t}, tendon length; l_{MTU}, muscle-tendon unit length; $\hat{l}$, normalized muscle length; $\hat{l}_{\mathrm{t}}$, normalized tendon length; $\hat{v}$, normalized muscle contraction velocity; $\hat{F}_{\mathrm{t}}(\hat{l}_{\mathrm{t}})$, normalized tendon force as a function of $\hat{l}_{\mathrm{t}}$; $\hat{F}_{\mathrm{a}}(\hat{l})$, normalized active muscle force as a function of $\hat{l}$; $\hat{F}_{\mathrm{p}}(\hat{l})$, normalized passive muscle force as a function of $\hat{l}$; $\hat{F}_{\mathrm{a}}(\hat{v})$, normalized active muscle force as a function of $\hat{v}$. Refer to Table 2.1 for definition of all symbols.

At the free end of the muscle belly, a massless tendon (SEE) was added to the model to make up the whole muscle-tendon unit. The tendon force-length relationship ($\hat{F}_{\mathrm{t}}(\hat{l}_{\mathrm{t}})$) was also modelled using Bézier curves (Ross et al., 2018) fitted to experimental data from Dick et al. (2016), and had an initial line with slope that connected the origin to the point on the curve where the normalized tendon force equaled 0.01. This property ensured that there was a unique tendon length for each tendon force. The tendon force, $F_{\mathrm{t}}(t)$, was calculated as follows:

$$F_{\mathrm{t}}(t) = F_0 \cdot \hat{F}_{\mathrm{t}}\left(\hat{l}_{\mathrm{t}}\right) \tag{2.8}$$

Since the force was transmitted from muscle to the end of the tendon, the muscle force ($F(t)$) was equal to its tendon force ($F_{\mathrm{t}}(t)$) throughout the movement task.

$$F(t) = F_{\mathrm{t}}(t) \tag{2.9}$$

The time-varying normalized muscle length ($\hat{l}(t)$) was calculated as the time-varying muscle length ($l(t)$), divided by the optimal muscle length (l_0):

$$\hat{l}(t) = \frac{l(t)}{l_0} \tag{2.10}$$

The normalized muscle contraction velocity ($\hat{v}(t)$) was calculated as the first derivative of normalized muscle length ($\hat{l}(t)$) normalized to the maximum unloaded muscle shortening velocity (v_0):

$$\hat{v}(t) = \frac{d\hat{l}(t)}{dt} \cdot \frac{1}{v_0} \tag{2.11}$$

The time-varying normalized tendon length ($\hat{l}_{\mathrm{t}}(t)$) was calculated as the tendon length divided by the slack tendon length ($l_{\mathrm{t,slack}}$) where the tendon length was equal to the difference between the MTU length and muscle length:

$$\hat{l}_{\mathrm{t}}(t) = \frac{l_{\mathrm{MTU}}(t) - l(t)}{l_{\mathrm{t,slack}}} \tag{2.12}$$

Substituting Equations 2.7 – 2.8 and 2.10 – 2.12 into Equation 2.9 gave:

$$F_0 \cdot \left(\hat{a}(t) \cdot \hat{F}_{\mathrm{a}}\left(\frac{l(t)}{l_0}\right) \cdot \hat{F}_{\mathrm{a}}\left(\frac{dl(t)}{dt} \cdot \frac{1}{l_0} \cdot \frac{1}{v_0}\right) + \hat{F}_{\mathrm{p}}\left(\frac{l(t)}{l_0}\right)\right) = F_0 \cdot \hat{F}_{\mathrm{t}}\left(\frac{l_{\mathrm{MTU}}(t) - l(t)}{l_{\mathrm{t,slack}}}\right) \tag{2.13}$$

The time-varying normalized muscle length ($\hat{l}(t)$) as well as the normalized tendon length ($\hat{l}_{\mathrm{t}}(t)$) were calculated from equation 2.13. Finally, the time-varying muscle force which equaled to the tendon force could be obtained by the tendon force-length relationship.

Mass-enhanced Hill-type muscle model

The muscle in the mass-enhanced model was split into n segments ($n = 16$) with an optimal segment length (l_0/n) evenly distributed from the optimal muscle length (l_0), and each segment contained a massless Hill-type model as described earlier. Between

the segments and between the last segment and tendon, there were n point masses divided homogeneously from the muscle mass, and each point mass was accelerated by its adjacent forces, either muscle ($F_i(t)$) or tendon force ($F_{\mathrm{t}}(t)$), which changed the position of each point mass ($x_i(t)$), where i is the segment number (Figure 2.3).

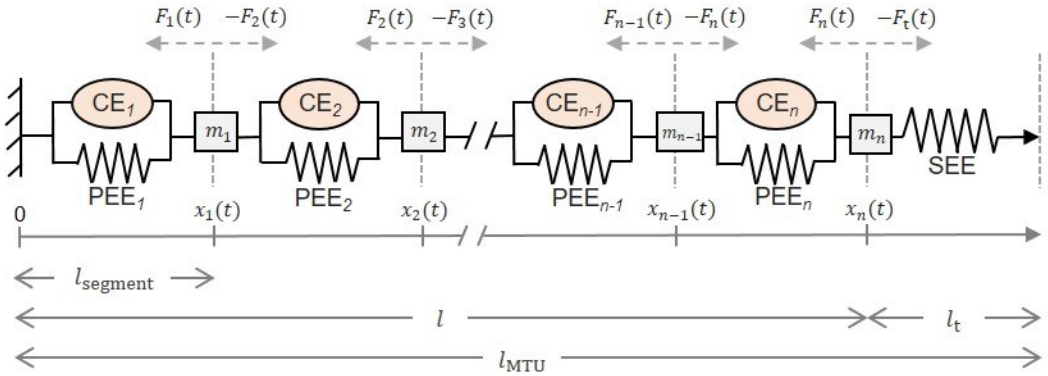

Figure 2.3. The mass-enhanced Hill-type muscle model.
The muscle is split into n segments with an optimal segment length (l_0/n) evenly distributed from the optimal muscle length (l_0), and each segment contains a Hill-type model as described earlier. Between the segments and between the last segment and tendon, there are n point masses (m_i) divided homogeneously from the muscle mass. Each point mass is accelerated by its adjacent components, either muscle actuators ($F_i(t)$) or tendon force ($F_{\mathrm{t}}(t)$), which changes the position of each point mass ($x_i(t)$). l, the muscle length; l_{t}, tendon length; l_{MTU}, muscle-tendon unit length; $n = 16$ in this study.

For each point mass, the resultant of the forces from the neighboring segments ($F_{i+1}(t)$ and $F_i(t)$) equaled to the product of mass (m_i) and its acceleration caused by that resultant force (Figure 2.3). For the last point mass (m_n), the resultant force acting on it came from the force of the n^{th} segment ($F_n(t)$) and the tendon force ($F_{\mathrm{t}}(t)$):

$$F_{i+1}(t) - F_i(t) = m_i \frac{d^2 x_i(t)}{dt^2} \tag{2.14}$$

$$F_{\mathrm{t}}(t) - F_n(t) = m_n \frac{d^2 x_n(t)}{dt^2} \tag{2.15}$$

where i is an integer starting from 1 to 15, and n is 16. Before the muscle was activated, the initial position of each point mass ($x_i(0)$) was given by:

$$x_i(0) = \left(\frac{l_{\mathrm{initial}}}{n}\right) \cdot i \tag{2.16}$$

By solving the above equations (Equations 2.8, 2.10 – 2.10, and 2.14 – 2.16), the positions of m_i, $x_i(t)$, and $\hat{l}_{\mathrm{t}}(t)$ could be determined. Consequently, tendon force was estimated

with the tendon force-length relationship (Dick et al., 2016), and the total external muscle force ($F(t)$) was equivalent to its tendon force ($F_{\mathrm{t}}(t)$) assuming the muscle force was transmitted through this in-series tendon to the end of the MTU.

2.3.4. Determination of optimal muscle Length

First, we calculated an estimated optimal muscle length ($l_{0,\mathrm{est}}$) and an estimated slack tendon length ($l_{\mathrm{t,slack,est}}$) by following equations:

$$l_{0,\mathrm{est}} = l_{0,\mathrm{MTU}} \cdot R_{\mathrm{m-to-MTU}} \tag{2.17}$$

$$l_{\mathrm{t,slack,est}} = l_{0,\mathrm{MTU}} \cdot (1 - R_{\mathrm{m-to-MTU}}) \tag{2.18}$$

where $R_{\mathrm{m-to-MTU}}$ is the muscle-to-MTU-length ratio for particular muscle (O'Brien et al., 2010; Kovács et al., 2020; van der Made et al., 2015). Subsequently, the actual optimal muscle length (l_0) and slack tendon length ($l_{\mathrm{t,slack}}$) for each muscle in both massless and mass-enhanced muscle models were determined by solving the following equation where muscle was relaxed and static, and the tendon force equaled to the passive muscle force:

$$l_0 = l_{0,\mathrm{est}} + e_1 \tag{2.19}$$

$$l_{\mathrm{t,slack}} = l_{\mathrm{t,slack,est}} - e_1 \tag{2.20}$$

$$F_0 \cdot \hat{F}_{\mathrm{t}}\left(\frac{l_{\mathrm{t,slack,est}}}{l_{\mathrm{t,slack}}}\right) = F_0 \cdot \hat{F}_{\mathrm{p}}\left(\frac{l_{0,\mathrm{est}}}{l_0}\right) \tag{2.21}$$

where e_1 is an error between an actual optimal value and an estimated optimal value.

2.3.5. Initial condition

To facilitate the computation of the models, an initial condition was created for each task in which muscle was relaxed (EMG intensity is set to be zero) and the initial MTU length ($l_{\mathrm{MTU,initial}}$) was constant for about five seconds. This initial MTU length of each muscle was assumed to be the median MTU length throughout the given task. This assumption could make sure the initial MTU length fell within the range of time-varying MTU length during the movement task. The estimated initial muscle length ($l_{\mathrm{initial,est}}$) and tendon length ($l_{\mathrm{t,initial,est}}$) were determined by:

$$l_{\mathrm{initial,est}} = l_{\mathrm{MTU,initial}} \cdot R_{\mathrm{m-to-MTU}} \tag{2.22}$$

$$l_{\mathrm{t,initial,est}} = l_{\mathrm{MTU,initial}} \cdot (1 - R_{\mathrm{m-to-MTU}}) \tag{2.23}$$

Then the actual initial muscle length (l_{initial}) and initial tendon length ($l_{\mathrm{t,initial}}$) were calculated by:

$$l_{\mathrm{initial}} = l_{\mathrm{initial,est}} + e_2 \tag{2.24}$$

$$l_{\mathrm{t,initial}} = l_{\mathrm{t,initial,est}} - e_2 \tag{2.25}$$

$$F_0 \cdot \hat{F}_{\mathrm{t}}\left(\frac{l_{\mathrm{t,initial,est}}}{l_{\mathrm{t,initial}}}\right) = F_0 \cdot \hat{F}_{\mathrm{p}}\left(\frac{l_{\mathrm{initial,est}}}{l_{\mathrm{initial}}}\right) \tag{2.26}$$

where e_2 is an error between an actual initial value and an estimated initial value.

2.3.6. Scaling

To test the mass effects, simulations were run for comparing muscles of different sizes with identical muscle geometric properties. Muscle sizes were changed by multiplying the MTU lengths by different scaling factors, 0.1, 1, and 10. As such, the muscle and tendon lengths were in proportional to the scaling factor, the muscle $PCSA_0$and thus muscle force were in proportion to the scaling factor squared, and V_{muscle} and mass were in proportion to the scaling factor cubed (Table 2.2).

Table 2.2 Multiplication factors.

Scale Factor	Length, velocity, acceleration	Area	Volume, mass	Stress	Maximum isometric force	Normalized length, velocity, acceleration	Normalized force
0.1	×0.1	$\times 0.1^2$	$\times 0.1^3$	×1	$\times 0.1^2$	×1	×1
1	× 1	$\times 1^2$	$\times 1^3$	×1	$\times 1^2$	×1	×1
10	×10	$\times 10^2$	$\times 10^3$	×1	$\times 10^2$	×1	×1

2.3.7. Comparisons of Predicted Muscle Performances

The muscle performance was evaluated by normalized muscle force ($\hat{F}(t)$) in this study, which was calculated as the muscle force ($F(t)$) normalized to the maximum isometric muscle force (F_0). $\hat{F}(t)$ predicted by mass-enhanced and massless Hill-type muscle models were compared for the 20 participants across muscles, tasks, scaled sizes. Data were analyzed for the final five cycles occurring between 15 to 25 seconds into the 30-second testing period. This approach allowed subjects to acclimate to the tasks and

provided the computer with the necessary time to compute the data and achieve a steady-state solution. For the sit-to-stand task, due to the extended duration required to complete one full cycle of movement, we specifically analyzed data from a single cycle occurring between 15 and 25 seconds into the testing period for computation.

To characterize the variation and correlation between predictions of the mass-enhanced and massless models, we computed the root-mean-squared error (RMSE) and coefficient of determination (r^2) between the two model-predicted forces as outcome measures. We conducted a general linear model ANOVA to ascertain differences in RMSE and r^2 between the two model-predicted forces (dependent variables) among scaled sizes (*N*=3), muscles (*N*=4), and tasks (*N*=4) (fixed independent variables) across subjects (*N*=20) (random variable) (IBM SPSS Statistics 29). Post-hoc analysis with least significant difference test (Meier, 2006) was used to examine the pairwise differences in RMSE and r^2 among groups. Significance was determined at the level of *P*<0.05, while data are presented as the mean ± standard error.

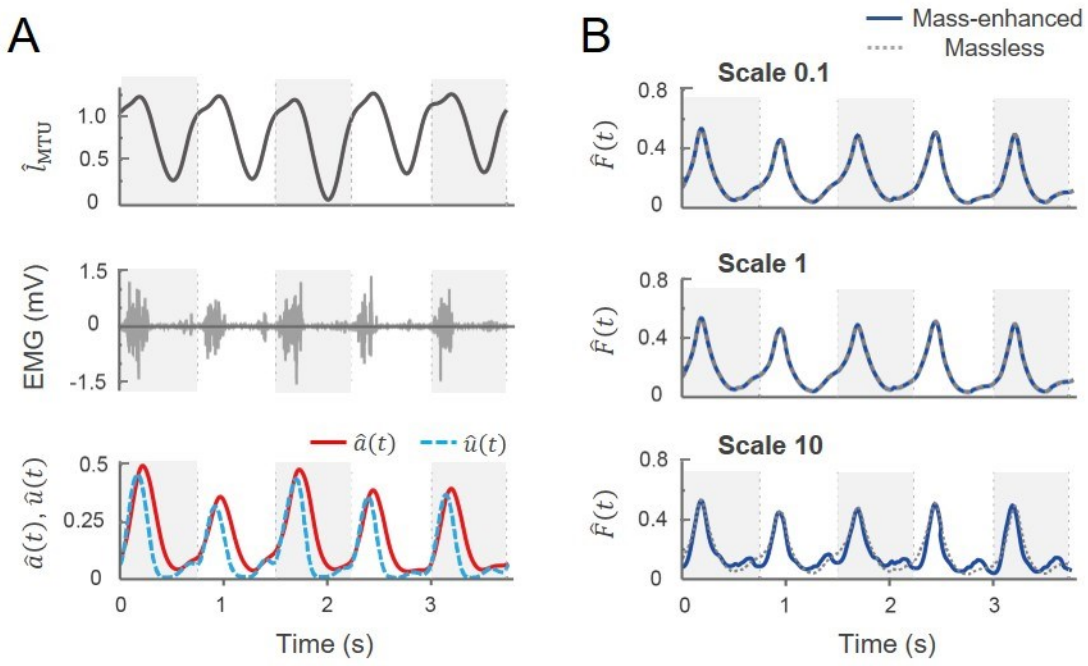

Figure 2.4. Sample raw traces and predicted muscle forces using massless and mass-enhanced muscle models at different scales.

Muscle-tendon unit (MTU) length normalized to its optimal length over time is shown in the top row of (A). Each grey or white block represents one movement cycle. The middle row shows raw electromyographic (EMG) data over time. The EMG data is converted to muscle excitation normalized to the maximum excitation ($\hat{u}(t)$) (blue, dashed) and muscle activation normalized to the maximum activation ($\hat{a}(t)$) (red, solid) over time, which are shown in the bottom row. Using

time-varying normalized MTU length and normalized activation level inputs, normalized muscle force ($\hat{F}(t)$) over time is computed with massless or mass-enhanced model. (B) depicts predicted time-varying muscle forces from both models across three scales. The predicted forces from both models overlap at scales 0.1 and 1, but at scale 10, a noticeable difference in predicted forces emerges between the models. The data is taken from right MG muscle of one representative subject during running task.

2.4. Results

For the mass-enhanced model, the predicted $\hat{F}(t)$ overlapped with the predicted $\hat{F}(t)$ of the massless model at both scales 0.1 and 1 (Figure 2.4B). However, at scale 10, the predicted $\hat{F}(t)$ showed more fluctuations, and a noticeable difference between the models emerged (Figure 2.4B, bottom row). Using the MG muscle during running as an example, the average $\hat{F}(t)$ per cycle for the mass-enhanced model was 20.71±0.40 % $\hat{F}_0$ at scale 10 (where $\hat{F}_0$ is the maximum normalized muscle force, which equals 1). In comparison, the average $\hat{F}(t)$ per cycle for the mass-enhanced model at scales 0.1 and 1, as well as the average $\hat{F}$ per cycle for the massless model at scales 0.1, 1, and 10, was consistent 21.60±0.43 % $\hat{F}_0$.

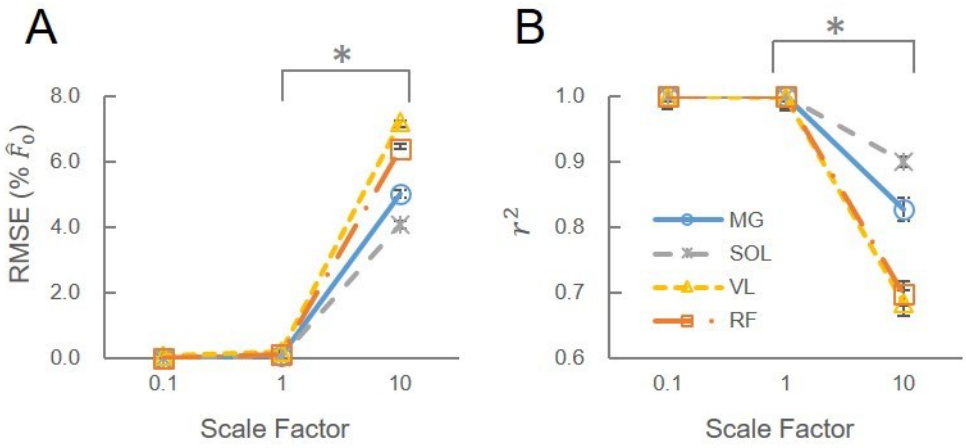

Figure 2.5. The mass (size) effect on the difference and correlation between massless and mass-enhanced model predictions of muscle force.
Here we consider the running task as representative. Each point represents the estimated marginal means of (A) root-mean-squared error (RMSE) and (B) coefficient of determination (r^2) between the two model-predicted forces for a particular muscle at a specific scale (0.1, 1, or 10). The small error bars, representing the standard error of the means, coincide with points indicating the mean values. These values are calculated using the average from the last five movement cycles of each subjects. (A) The RMSE values at scales 0.1 and 1 are relatively small, while the RMSE values at scale 10 is notably larger across all tested muscles (*: P<0.001). (B) The r^2 exhibits a substantial decrease at scale 10 in comparison to scale 1 across all muscles (*: P<0.001).

The ANOVA tests showed a significant effect of scale on the RMSE (P<0.001) and the r^2 (P<0.001) for the differences in normalized muscle forces. The difference of forces predicted by both models, using RMSE and r^2, revealed larger discrepancies at scale 10 compared to scales 0.1 and 1. When averaged across subjects in running task, the RMSE values at scales 0.1 and 1 were relatively small, with the largest recorded at 0.177±0.046 % $\hat{F}_0$ for VL at scale 1. Conversely, RMSE at scale 10 was notably larger across all tested muscles in running , ranging from 4.062±0.125 % $\hat{F}_0$ for SOL to 7.228±0.181 % $\hat{F}_0$ for VL (Figure 2.5). The post-hoc analysis showed significant differences between conditions at scales 1 and 10 (P<0.001 for the four tested muscles). However, differences between scales 0.1 and 1 conditions were not significant for most muscles in running, except for RF (P =0.02). For the correlation between the models, the r^2 values exhibited a substantial and significant decrease at scale 10 in comparison to scale 1 across all muscles (P<0.001), ranging from 0.900±0.007 for SOL to 0.684±0.020 for VL. In contrast, the r^2 values at scales 0.1 and 1 surpassed 0.999 across all muscles and were not significantly different. This observed pattern, larger RMSE and lower r^2 at scale 10 compared to scales 0.1 and 1, persisted consistently across all examined muscles and tasks (Figure 2.6). The highest RMSE and the lowest r^2 values across muscles and tasks were recorded at 7.228±0.181 % $\hat{F}_0$ for VL in running, and 0.392±0.031 for RF in walking, respectively. However, the variance across different scales was not homogeneous and increased with scale factor, violating one of the assumptions of ANOVA. Specifically, the scale-specific overall RMSE mean and standard error values, averaged across subjects, muscles, and tasks, were 0.007±0.003 % $\hat{F}_0$ at scale 0.1, increased to 0.089±0.008 % $\hat{F}_0$ at scale 1 (P=0.145), and significantly rose to 4.631±0.068 % $\hat{F}_0$ at scale 10 (P <0.001). Therefore, we applied a Log-transformation to the RMSE data to repeat the ANOVA.

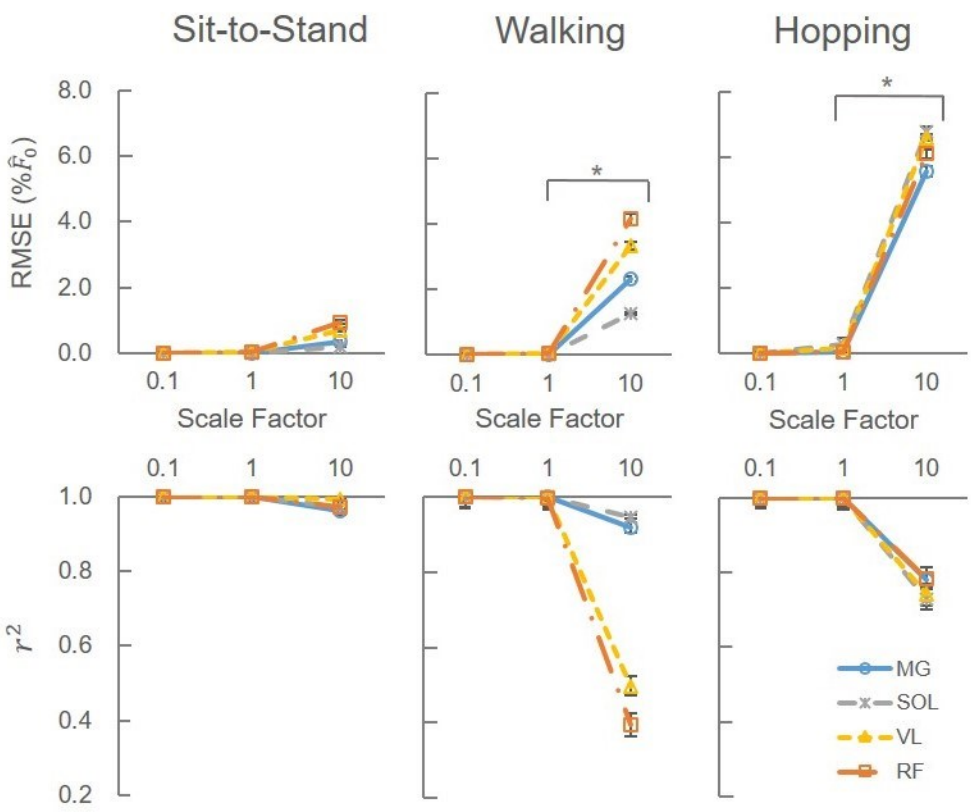

Figure 2.6. The mass (size) effect on the difference and correlation between massless and mass-enhanced model predictions of muscle forces at sit-to-stand, walking, and hopping tasks.

The RMSE for each muscle across various tasks remains relatively small at scales 0.1 and 1, with the highest value recorded at 0.310±0.076 % $\hat{F}_0$ for the SOL muscle during hopping at scale 1. Concurrently, the coefficient of determination (r^2) consistently remains no less than 0.999 at scales 0.1 and 1. However, a notable increase in RMSE is observed at scale 10 across different muscles and tasks, coinciding with comparatively lower r^2 values when compared to scales 0.1 and 1. * indicates significance across all muscles (*P*<0.001).

Figure 2.7. The interaction between effects of scaled muscle mass (size), task, and muscle on the difference between model-predicted forces.

The Y-axis markers have been adjusted to represent the logarithmic values of RMSE between predictions of muscle force in massless and mass-enhanced models. Each plotted point denotes the average logarithmic RMSE value across subjects for a particular muscle engaged in a specific task and scale. Across different scales, the scale-specific overall logarithmic RMSE values, represented by the boundary of the blue background, are calculated by averaging across various muscles and tasks within each specific scale. These values illustrate an ascending trend corresponding to scale increments. At identical scales, the average logarithmic RMSE values consistently exhibit higher magnitudes during running and hopping tasks in contrast to walking or sit-to-stand tasks for any given muscle across various scales. Additionally, the ranking of muscles based on RMSE varies between tasks.

The ANOVA tests for the Log-transformed RMSE in $\hat{F}(t)$ between the mass-enhanced and massless models (Figure 2.7) again showed a significant effect of scale. The scale-specific overall logarithmic value of RMSE (depicted by the boundary of the blue background in Figure 2.7), calculated by averaging across various muscles and tasks within each specific scale, demonstrated an ascending trend corresponding to scale increments, and exhibited significant differences between scales 0.1 and 1 as well as between 1 and 10 in post-hoc analysis (P<0.001), indicating persistent mass effects in small-sized muscles. The logarithmic values of RMSE and standard error, averaged across subjects, muscles, and tasks, were −2.794±0.320, −1.354±0.442, 0.566±0.355, at scale 0.1, 1, and 10, respectively.

At identical scales, the values of RMSE and standard error consistently exhibited higher magnitudes during running and hopping tasks in contrast to walking or sit-to-stand tasks for any given muscle across various scales. For example, in the SOL muscle at scale 1, the RMSE values were 0.310±0.076 % $\hat{F}_0$ and 0.046±0.002 % $\hat{F}_0$ in hopping and running, respectively, and were 0.013±0.001 % $\hat{F}_0$ and 0.002±0.000 % $\hat{F}_0$ in walking and sit-to-stand, respectively. Significant differences in logarithmic RMSE values across

muscles were observed for any given scale in pairwise comparisons between hopping and walking (P<0.001), hopping and sit-to-stand tasks (P<0.001), running and walking (P<0.001), as well as running and sit-to-stand tasks (P=0.01). The mass effects were thus more pronounced in running and hopping tasks compared to walking and sit-to-stand tasks.

2.5. Discussion

Previous modeling studies have highlighted that considering muscle mass can significantly affect predictions of muscle performance. These alterations include reductions in maximum shortening velocities (Meier & Blickhan, 2000; Böl & Reese, 2008; Ross & Wakeling, 2016), as well as changes in mechanical work per cycle (Ross et al., 2018b). Notably, this mass effect on muscle performance becomes more pronounced at submaximal activation levels (Ross & Wakeling, 2016) and when scaling muscles to larger sizes (Günther et al., 2012; Ross & Wakeling, 2016; Ross et al., 2018b). To ascertain the consistency of this mass effect across both modelling and animal studies, Ross and colleagues (2020) looked into the mass effect within rat plantaris muscle, revealing that the addition of greater mass led to a reduction in mass-specific mechanical work per cycle compared to the unloaded trials where no additional mass was applied. Moreover, increased muscle strain corresponded to reduced work per cycle in comparison to unloaded trials at the same strain. This might be attributed to the potentially higher acceleration of the muscle mass experienced during higher strain conditions. The *in situ* study supported that the tissue inertia affected the muscle performance in real muscle. Despite these findings, the mass effect has yet to be experimentally tested in human muscles during locomotion. There remained uncertainty regarding whether muscle mass has a significant impact on the contractile properties of human-sized muscles during daily movement. Furthermore, the extent of variation in predictions of muscle performance between models that consider and those that disregard muscle mass remained unknown.

Since it is not possible to manipulate the living human muscle mass in experiment, we collected the participants' kinematic data during locomotion to estimate the MTU length, and then scaled the length to different sizes. As the geometric proportions of the model remained constant, while length scaled with the scaling factor, PSCA scaled with the square of the scaling factor, and the volume and mass scaled with the cube of the scaling factor (Table 2.2). These scaled geometric data were used to drive both a massless and

mass-enhanced Hill-type models (Figure 2.2 and 2.3) for comparison of muscle performance predictions. This is the first study of its kind simulating human experimental muscle contractions in movements of daily activities with a mass-enhanced model, pioneering the assessment of mass effects on muscle performance predictions. The outcome would help determine if the difference in muscle performance predictions between the two models could be negligible in human-sized muscles during daily locomotion, and how the discrepancy would vary with changes in muscle mass.

2.5.1. Mass effects on the predicted forces

Although the predicted muscle forces of the massless model increased in proportion to the scale factor squared, we found that the predicted normalized forces remained constant across scales (Figure 2.4B). This can be explained by that in our massless model, normalized muscle force mainly depends on the force-length, force-velocity, and tendon force-length properties, where the force, length and velocity are all normalized. Additionally, the input normalized length and velocity do not change with scale factor. Consequently, the output values of normalized force in the massless model stay constant regardless of the scaled size. In contrast, the mass-enhanced model consists of point masses between muscle segments and the tendon (Figure 2.3). When a muscle is activated to generate force to move a point mass, the inertial resistance due to the mass affects the balance between forces of muscle segments or tendon adjacent to the point mass. The neighboring segment lengths and tendon length therefore change in a different pattern to balance the forces in series. This results in an asynchronous shortening-lengthening movement of each muscle segment and tendon, leading to varied normalized segment lengths (Figure 2.8). Consequently, the predicted normalized muscle force of the mass-enhanced model may differ from that of the massless model. Furthermore, when the muscle size (mass) and/or acceleration is greater, greater inertial resistance amplifies discrepancies between adjacent forces acting on the mass, thereby enlarging the difference of predicted forces.

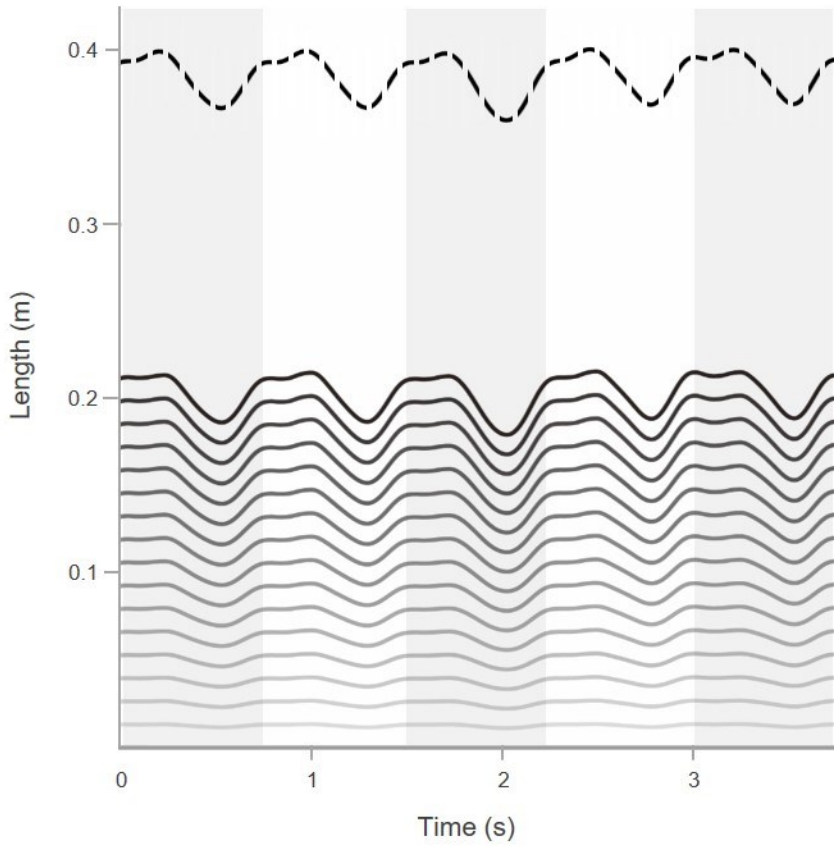

Figure 2.8. Time-varying length of muscle segments and muscle-tendon unit (MTU).

The dashed line represents the time-varying MTU length, while the solid lines, ranging from the bottom (lightest grey) to the top (darkest grey), depict the time-varying lengths of the 1st to the 16th muscle segments in order. Each grey or white block represents one movement cycle. The data is taken from right MG muscle of one representative subject during running task.

In this study, we used the RMSE between predicted normalized forces of a mass-enhanced model and a massless model to represent effects of muscle mass on the predicted muscle forces. Larger RMSE values indicated greater mass effects. A significant difference in RMSE values between the studied groups signified different magnitudes of mass effects between groups. Our results consistently revealed significantly larger RMSE values at a scale of 10 compared to scales 1 and 0.1 across muscles and tasks (P<0.001). In contrast, the post-hoc analysis did not show a significant difference in RMSE values between scales 1 and 0.1. This lack of significance may be attributed to the relatively smaller RMSE values observed at scales 0.1 and 1, or the heterogeneity in variance among the groups, potentially obscuring the difference between scales 0.1 and 1. When log-transformed RMSE were considered, significant differences emerged between scales 1 and 0.1 across muscles for all tasks (P<0.001). Taken together, these results suggest

that significant mass effects occur across all tested scales (0.1 to 10), however, the magnitude of these effects may only become functionally important at scales larger than 1 for the activities of daily living tested here.

We also found some other features were only present at scale 10 when predicted forces were averaged across muscles and tasks. Average $\hat{F}(t)$ per cycle predicted by the mass-enhanced model was lower at scale 10 compared to those at other scales (P<0.001), with 15.534, 15.489, 15.222 % $\hat{F}_0$ at scale 0.1, 1 and 10. The mass-enhanced model exhibited a peak force occurring 2.12 % of the cycle earlier than the massless model (P<0.001), suggesting that mass effects could contribute to an earlier peak force. This observation might align with a previous in situ study (Ross et al., 2020) that demonstrated an earlier force peak at higher strain compared to lower strain, potentially attributable to increased acceleration and, consequently, greater mass effects at higher strain levels.

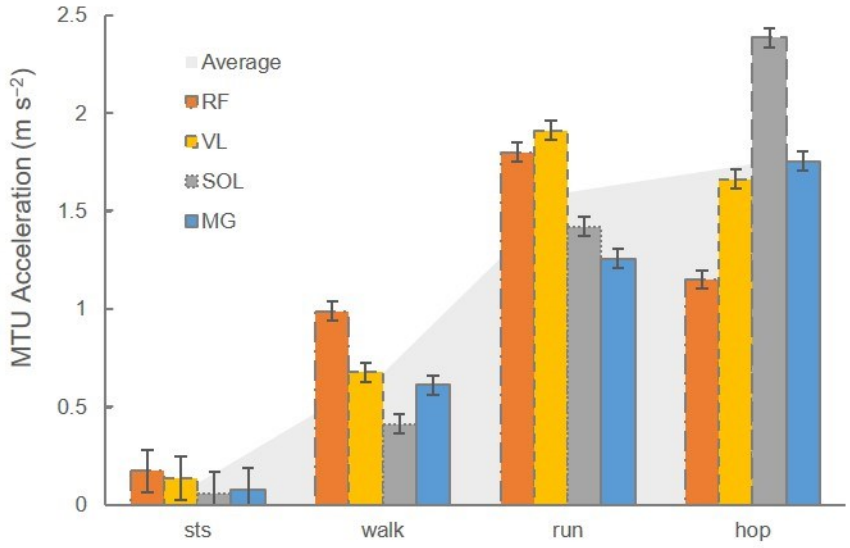

Figure 2.9. Muscle-tendon unit (MTU) acceleration in the tested muscles across tasks at scale 1.

MTU acceleration is calculated as the root-mean-squared value of instantaneous MTU acceleration values per cycle. The boundary of Grey background represents the MTU acceleration averaged across muscles in each task. Tasks were ranked by MTU acceleration averaged across muscles from lowest to highest.

2.5.2. Mass effects in different tasks and muscles

At the same scale, we consistently observed higher RMSE values for running and hopping tasks compared to walking and sit-to-stand tasks for any muscle or scale. As the models differ only in the inclusion of mass effects, given the same scale factor, varying

MTU accelerations in different tasks likely contribute to the RMSE differences observed. MTU acceleration is calculated as the root-mean-squared values of instantaneous MTU acceleration for each cycle. We found that when considering the average across muscles, tasks were ranked by MTU acceleration from lowest to highest as follows: sit-to-stand, walking, running, hopping (Figure 2.9). Significant differences among these tasks were revealed through pairwise comparisons (P<0.001), and this ranking aligned with that determined by RMSE. The coefficient of determination between MTU acceleration and RMSE values was 0.204 (P<0.001) across subjects and tasks. This suggests that RMSE value significantly correlates MTU acceleration but can be affect by other factors. Specifically examining the calf muscles (SOL, MG), both MTU acceleration and RMSE consistently showed sit-to-stand with the lowest values, followed by walking, then running, and finally hopping with the highest values. Conversely, for quadriceps (RF, VL), the hierarchy of values across tasks was observed as sit-to-stand with the lowest values, followed by walking, hopping, and running with the highest values. Among these muscles, high correlation between MTU acceleration and RMSE was shown for RF and MG (coefficient of determination were 0.677 and 0.955, respectively; P<0.001). These findings might support the explanation that MTU acceleration could affect the difference of muscle predictions between the two models. In other words, mass has greater effects on the activities with higher accelerations (occurring during the high-cadence movements). However, further investigation is needed into other factors, such as muscle activation levels, which may also contribute to the differences in RMSE among tasks.

2.5.3. Limitations of our model assumptions

The primary goal of this study was to examine the difference of predicted forces between 1D mass-enhanced and massless models and how this difference changed with scaled muscle size. In order to focus on the investigation of mass effects on the muscle performance predictions, we controlled effects from other potential impact factors by simplifying the muscle architecture with assumptions that muscles have no aponeurosis or internal tendon, have constant volumes depending on subject's mass and height (Handsfield et al., 2014), have parallel fibres aligned with contraction direction, and have fibre length equivalent to the muscle belly length, and each muscle has a fixed end and a free end connected with its own tendon. Additionally, the influence of fibre types (Lee et al., 2011; Wakeling et al., 2012), history-dependent effects (Abbott & Aubert, 1952; Edman

et al., 1982; Meijer et al., 1998; Morgan et al., 2000; Herzog & Leonard, 2000, 2002), three-dimensional effects (Meier & Blickhan, 2000; Böl & Reese, 2008; Ross et al., 2018b), and viscous damping effects (Gasser & Hill, 1924; Levin & Wyman, 1927; Heerkens et al., 1987; Syme, 1990; Best et al., 1994) were also ignored in this study to reduce computation complexity.

We did not account for the history-dependent effect since it is believed to stem from mechanisms at the cross-bridge level (Herzog et al., 2012), which are not directly influenced by muscle mass dynamics. Regarding the viscous (velocity-dependent) damping effect, the inclusion of a damping element has been used to simulate tissue viscosity within muscles (Hatze, 1977; Günther et al., 2007) or enhance the numerical stability of computations while maintaining force balance between muscle and tendon (Millard et al., 2013). However, in our model, we chose to disregard this effect as its incorporation had the potential to diminish length changes in muscle and tendon, thereby reducing the predicted muscle forces. Consequently, both these effects were excluded from our model formulation. It is likely that their omission did not significantly alter the primary conclusions drawn from our modeling results.

We used a one-element model with a single fibre-type without considering the effects of fibre types because previous studies showed only minor differences of predictive performances between one-element and two-element models with two fibre-types (Dick et al., 2017). Besides, the two-element model performed better than the one-element model at high cadence (>100 r.p.m.) (Dick et al., 2017), but most of our tasks were not high-cadence movements. Although a previous study showed that using a maximum unloaded muscle shortening velocity (v_0= 10 s^{-1}) typical for fast fibres resulted in greater mass effects (Ross et al., 2018b; Ross & Wakeling, 2021) compared to that for slow fibres, we assumed that only slow fibres were involved in our tasks because the tasks were low-intensity daily activities and were conducted at a casual, comfortable level, where the recruitment of slow fibres is likely predominant. However, in hopping, which had an average cadence of 107.1 r.p.m. and was relatively intense compared to other tasks, it might be beneficial to incorporate the two-element model, or a faster v_0, to better reflect the intrinsic properties of the recruited muscle fibres. Furthermore, the proportion of slow and fast twitch fibres varies among muscles. For example, SOL muscle contains 70 % of slow fibres while gastrocnemius and VL has a lower proportion of slow fibres (about 50 %

and 32 %, respectively) (Edgerton et al., 1975). Therefore, using the fast fibres in muscles having a lower proportion of slow fibres might result in a better prediction.

The inclusion of a tendon in mass-enhanced models has been shown to mitigate the decline in mechanical work output per cycle associated with increased mass (Ross & Wakeling, 2021). An intermediate, optimal tendon stiffness has been identified, leading to the highest work output (Ross & Wakeling, 2021). This optimal stiffness is influenced by scaled muscle sizes and the timing of muscle excitation in relation to the start of MTU shortening (Lichtwark et al., 2005; Lichtwark et al., 2010; Ettema, 2001; Sawicki et al., 2015). However, the tendon force-length property, using Bézier curves (Ross et al., 2018a) fitted to experimental data (Dick et al., 2016), might not fully represent the diverse tendon characteristics of all muscles.This property was derived from experimental measurements specifically focusing on the Achilles tendon (AT) at a fixed knee angle. It did not consider the influence of varying knee angles on the MTU length during movement. Moreover, the AT tendon property might not accurately depict the properties of other tendons due to the inherent differences in function, structure, cross-sectional area (CSA), and mechanical properties among tendons (Cutts et al., 1991; Magnusson et al., 2008; Matson et al., 2012; Wang et al., 2012). For instance, while the human TA tendon exhibits a Young's modulus of approximately 1200 MPa (Maganaris & Paul, 1999), the patellar tendon records a value of 660 MPa (Johnson et al., 1994). A tendon with greater stiffness necessitates a higher force for stretching, consequently altering the tendon's force-length relationships (Geremia et al., 2018). Nonetheless, although we only used one tendon property in the models, it should not affect our main aims of presenting the difference in predicted forces between mass-enhanced and massless models.

1D Hill-type muscle models overlook the 3D shape and structure of muscles, potentially causing differences between predicted and actual mass effects. Muscle mass is not uniformly distributed; it is largest around the middle and tapers towards the ends, varying among muscles (Fukunaga et al., 1992; Morse et al., 2007; Erskine et al., 2009; Cotofana et al., 2010; Maden-Wilkinson et al., 2013). When muscles contract, they expand in width and thickness, altering where the largest mass is located (Hodgson et al., 2006; Baskin & Paolini, 1967). Besides, regional muscle activation may also alter inactive tissue inertia during submaximal contractions (English, 1984; Pratt & Loeb, 1991; Boggs & Dial, 1993; Schieber, 1993; Soman et al., 2005; Wakeling, 2008; Kinugasa et al., 2011; Hodson-Tole et al., 2013). In pennate muscles, muscle fibres rotate during contraction,

causing different shortening speeds relative to the muscle belly (Azizi et al., 2008). Our 1D model does not account for muscle shape changes or rotation-related effects. It only focuses on 1D muscle dynamics and kinematics along the muscle's length, ignoring tissue mass influences in other directions. Studies have suggested that including 3D tissue properties results in greater mass effects in terms of decreases in maximum shortening velocity and mechanical work per cycle (Meier & Blickhan, 2000; Böl & Reese, 2008; Ross et al., 2018b; Ross et al., 2021). Though direct comparisons between 1D and 3D mass effects are lacking, incorporation of the mass effects in all directions likely further reduce predicted muscle work output in human muscle. Further exploration for tissue mass effects on muscle function in 3D is needed for a comprehensive view of overall muscle behavior.

2.6. Conclusion

This study marks the first to use a mass-enhanced muscle model for simulating human muscle contractions during various daily activities. When we scaled muscles to different sizes, we discovered that mass effects, observed through the root-mean-squared errors (RMSE) between predicted forces in a mass-enhanced model and a massless one, were minor and functionally insignificant for smaller muscles. However, mass effects for these activities of daily living became more pronounced as the muscles exceeded human size. This trend of mass effects increasing with scaled size remained consistent across different muscles and daily activities. Furthermore, mass effects were more pronounced in running and hopping compared to walking and sit-to-stand tasks for all muscles tested. This difference may be attributed to the higher acceleration of muscle mass and consequent greater mass effects in these higher-cadence activities. These findings suggest that while mass effects can significantly influence muscle performance during daily human movement, their impact is minimal in human-sized or smaller muscles during slower activities. However, they become more apparent at larger scaled sizes and are influenced by the movement's cadence.

Chapter 3.

Effects of muscle mass on muscle performance predictions in human during cycling

3.1. Abstract

Muscle mass is recognized as a factor influencing muscle contractile performance, contributing to prediction errors in human muscle function during locomotion. However, the errors found in daily activities, characterized by low acceleration, are minimal and functionally insignificant in human-sized muscles. The impact of higher-cadence cyclic movement on potential errors, stemming from greater mass effects in human muscles, remains unknown. In this study, we simulated human muscles during cycling and explored how the muscle mass effect interacts with various scaled muscle sizes and diverse pedaling conditions, influencing predicted muscle performances. We used comprehensive sets of kinematic, kinetic, and electromyographic (EMG) data in lower limb muscles during various cycling conditions from twenty participants. We compared the normalized muscle force, volume-specific power, and volume-specific work output per cycle predicted by both mass-enhanced and massless muscle models across different scaled muscle masses, cycling conditions, and muscles. The root-mean-squared errors (RMSE) in predicted force and power between models served as the primary outcomes to indicate mass effects. The results revealed an exponential increase in prediction errors with scaled muscle mass, with an exponent of approximately 2. Errors could exceed 5 % in predicted forces for muscles 6^3 times greater than their original mass, with the quadriceps consistently displaying larger RMSE compared to calf muscles. While higher cadence cycling led to greater RMSE values, crank load showed no significant effect on RMSE values. Additionally, greater muscle mass resulted in a higher decrease in volume-specific net work output per cycle. In conclusion, muscle mass emerges as a crucial determinant of skeletal muscle behavior, particularly in muscles larger than human-sized muscles, especially during high-cadence movement.

3.2. Introduction

Skeletal muscles play a crucial role in enabling movement for both humans and animals by generating forces and mechanical work. Yet, directly measuring muscle function in living humans during movement is a considerable challenge. As a result, much of our understanding about large human muscles is derived from models based on experiments conducted on controlled, fully activated, isolated single fibres, or small muscles. These models operate under the assumption that large muscles and small fibres possess similar intrinsic properties, irrespective of their sizes or masses. Among these models, the Hill-type muscle model holds significance as one of the most extensively used for predicting muscle function. This model operates on the fundamental assumption that when a muscle is scaled up, the force it produces will proportionally scale with its cross-sectional area. It suggests that mass-specific power and mass-specific work per movement cycle will remain constant (Zajac, 1989). However, this assumption might have limitations due to the inertial resistance caused by muscle mass, which is a factor not included in Hill-type muscle models.

Recent research suggests that the internal load of muscle tissues can create inertial resistance, slowing down the rate of force development (Günther et al., 2012) and the maximum shortening speed of entire muscles (Ross & Wakeling, 2016). This mass effect is more prominent in larger muscles (Böl & Reese, 2008; Ross & Wakeling, 2016), especially during submaximal contractions, where inactive fibres may hinder contraction speed without contributing to contractile force (Josephson & Edman, 1988; Holt et al., 2014; Ross & Wakeling, 2016). Moreover, this inertial resistance has been observed to decrease the mechanical work output per cycle of muscles during both simulated (Ross et al., 2018b) and in situ (Ross et al., 2020; Ross & Wakeling, 2021) cyclic contractions.

To examine the altered dynamics of muscle contraction and performance influenced by the mass effect, we utilized mass-enhanced Hill-type muscle models in simulation studies (Günther et al., 2012; Ross & Wakeling, 2016; Ross et al., 2018a; Ross et al., 2020; Ross & Wakeling, 2021). This sophisticated model incorporates discrete point masses along the muscle's length, controlled by Hill-type actuators. In our investigation outlined in Chapter 2, we applied this model to analyze lower limb muscles in humans during activities of daily living, including walking and running. Our aim was to discern differences in predicted muscle behaviors when using mass-enhanced versus massless

Hill-type muscle models. Our results showed increasing disparities in predicted normalized forces as muscle size increased. Notably, during running tasks, the vastus lateralis (VL) muscle scaled up to one thousand times its original mass exhibited the most substantial disparity of 7.228±0.181 % $\hat{F}_0$. At the VL muscle's original size, the mass-enhanced model predicted a small but significant difference in time-varying forces compared to the massless model (RMSE 0.177±0.046 % $\hat{F}_0$). Furthermore, we observed more pronounced mass effects during running and hopping activities in comparison to walking and sit-to-stand tasks across all examined muscles. Despite the distinct kinematics of these tasks, our findings suggested intriguing possibilities. They hinted that mass effects of the muscle tissue itself might not be functionally important in daily movements of human-sized muscles due to their relatively low acceleration. However, muscles involved in high-cadence cyclic movements, characterized by increased acceleration, might display a more prominent mass effect. This might be one of the reasons that differences between the forces predicted by massless models and those estimated through ultrasound techniques are greater during high-cadence cycling, as reported in a study by Dick and her colleagues (2017).

In this study, we aimed to investigate the mass effects on human muscle performances during high-cadence cyclic movements to see if the mass effects were more substantial than those for the activities of daily living, due to their higher accelerations. To explore this, we utilized cycling on a stationary bicycle as a means to delve into high-cadence cyclic movement and its influence on mass effects. Cycling, as a controlled activity, presented advantages by facilitating precise manipulation of mechanical demands. This allowed for independent adjustments of external crank torque and pedaling cadence while maintaining consistent kinematics, a level of experimental control that is often challenging in studies focusing on gait (Hull & Jorge, 1985). Our approach involved conducting musculoskeletal simulations based on experimental muscle contractions during cycling. Specifically, we compared the muscle performances predicted by a mass-enhanced model and a massless muscle model. The primary objective was to investigate how the muscle mass effect interacts with various scaled muscle sizes and diverse pedaling conditions in the predicted human muscle performances. We hypothesized that the effect of the muscle mass on the predicted muscle force would increase as the cycling cadence increased. Furthermore, considering the absence of experimental validation of mass effects on mechanical work in human muscles, our aim was to predict muscle work

outputs using the mass-enhanced model. We hypothesized that under the same cycling conditions, muscle mass would lead to a reduction in the predicted volume-specific mechanical work per cycle compared to predictions from a mass-less muscle model.

3.3. Methods

3.3.1. Experimental data collection

Comprehensive sets of kinematic, kinetic, and electromyographic (EMG) data were previously collected from 20 competitive cyclists (gender ratio: female to male = 1:1; mean age: 30±7.3 years; average weight: 70.5±10.5 kg; mean height: 173.5±7.5 cm; mean±s.d.) as reported in Dick et al. (2016). The participation of all subjects was preceded by obtaining informed consent, and the study protocol obtained ethical approval from the ethics committees at Simon Fraser University and Harvard University.

Each cyclist engaged in a cycling protocol involving independent adjustments of crank torque and pedaling cadence across eleven distinct conditions (five of them are reported in this study). These conditions comprised varying crank torque levels at a consistent cadence of 80 rpm, specifically 13-14, 26, 32, and 44 N m, and diverse cadences of 60, 100, 120, and 140 rpm at a constant crank torque of 13 N m. The corresponding average crank power outputs for these pedaling conditions were 115 W, 220 W, 270 W, 370 W, 80 W, 135 W, 160 W, and 190 W. In addition to these trials, data for “maximum effort” sprint trials (high crank load and cadence) and static calibration trials were collected for normalizing muscles’ EMG intensities and scaling a subject-specific musculoskeletal model, respectively. Trials assessing dynamic hip range of motion were also conducted to determine subjects’ hip centers, as detailed in the previous study (Dick et al., 2016).

During each trial, the 3D trajectories of 32 LED markers, normal and radial pedal reaction forces to the crank, and surface EMG patterns from 10 left lower-limb muscles were recorded. Markers were tracked at a sampling rate of 100 Hz through an optical motion capture system (Certus Optotrak, NDI, Waterloo, ON, Canada), and their specific placement locations were detailed in Dick et al. (2016). Reaction forces were recorded bilaterally at 2000 Hz using clipless instrumented pedals (Powerforce, Radlabor, Freiburg, Germany) fixed to rigid sandals worn by the cyclist. Bipolar Ag/AgCl surface EMG

electrodes (10mm diameter, 21mm spacing; Norotrode; Myotronics, Kent, USA) were placed over the mid-bellies of medial gastrocnemius (MG), soleus (SOL), vastus lateralis (VL), rectus femoris (RF), and other six muscles (not reported in this study). EMG signals were pre-amplified (gain 1000-5000), band-pass filtered (bandwidth 10–500Hz; Biovision, Wehrheim, Germany), and sampled at 2000 Hz as described elsewhere (Dick et al., 2016).

3.3.2. Muscle model formulations

The models used in this study included one-dimensional (1D) massless and mass-enhanced Hill-type muscle models, which were described in details in Chapter 2. In brief, the muscles were assumed to (1) have no aponeurosis or internal tendon, (2) have constant volumes depending on subject's mass and height (Handsfield et al., 2014), (3) have parallel fibres aligned with the contraction direction of the muscle, and thus having fibre length equivalent to the muscle belly length, (4) and have a fixed end and a free end. The muscle force ($F(t)$) is assumed to be equal to its tendon force ($F_{\mathrm{t}}(t)$) throughout the movement task, under the assumption that force is transmitted completely from the muscle to the end of the tendon. Furthermore, the maximum muscle isometric stress (σ_0= 225 kPa; estimated from literature of Medler, 2002), muscle density (ρ = 1060 kg m^{-3}; Mendez & Keys, 1960), and maximum unloaded muscle shortening velocity (v_0= 10 s^{-1}; Wakeling et al., 2012) were assumed constant.

The massless Hill-type muscle model comprised a contractile element (CE) and a parallel elastic element (PEE) (Figure 3.1B). The CE normalized force was determined by muscle normalized activation ($\hat{a}(t)$), active force-length ($\hat{F}_{\mathrm{a}}\left(\hat{l}(t)\right)$), and active force-velocity relationships ($\hat{F}_{\mathrm{a}}\left(\frac{d\hat{l}(t)}{dt}\cdot\frac{1}{v_0}\right)$), while the PEE normalized force was solely influenced by the passive muscle force-length ($\hat{F}_{\mathrm{p}}\left(\hat{l}(t)\right)$) relationship (Figure 3.1C). These relationships were based on normalized values of force, length, and velocity. Force is normalized to its maximum isometric force, velocity is normalized to the maximum unloaded muscle shortening velocity, and length is normalized to its optimal length (indicated by a hat symbol to denote normalization). The relationships were built using Bézier curves (REF Steph's paper here) fitted to experimental data for CE normalized forces (Winters et al., 2011) and for PEE normalized forces (Roots et al., 2007). Additionally, the model was connected to a massless tendon (serial elastic element, SEE)

at the free end. The tendon force-length property ($\hat{F}_{\mathrm{t}}(\hat{l}_{\mathrm{t}}(t))$), which also depicted normalized force and length relationship, was established using Bézier curves (Ross et al., 2018) fitted to human Achilles tendon data (Dick et al., 2016), and had an initial slope instead of horizontal line on the tendon force-length curve to facilitate computation.

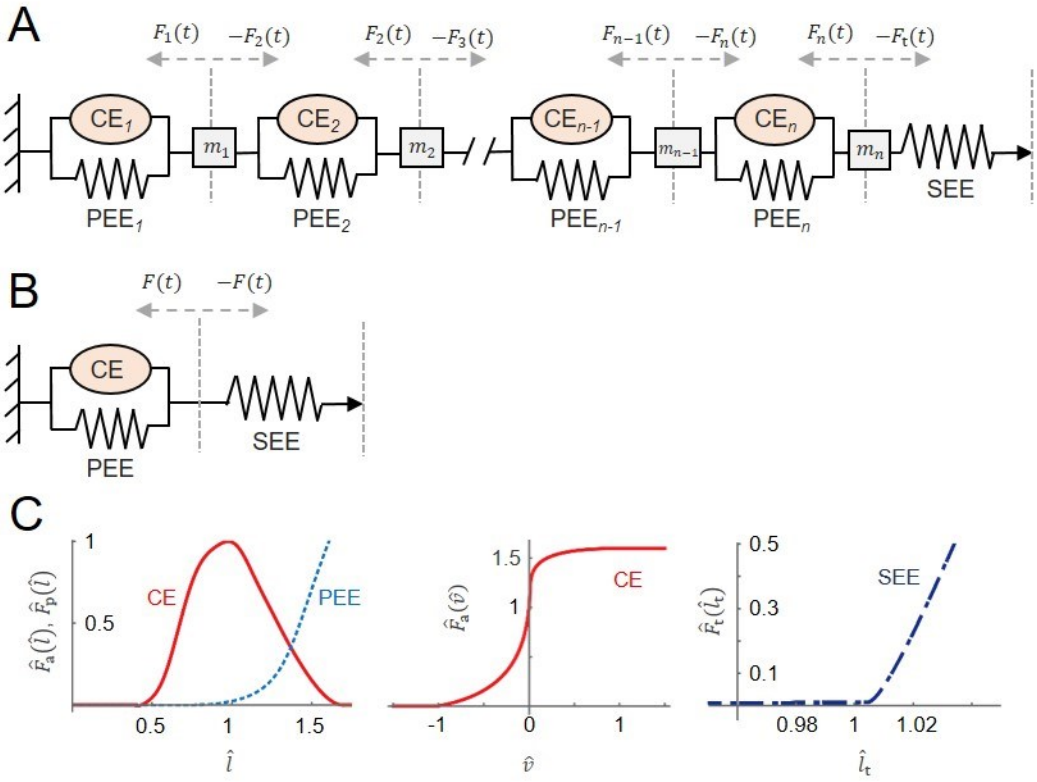

Figure 3.1. Muscle models used to simulate experimental contraction cycles.
The model consisted of an active muscle component (CE, contractile element), a passive muscle component (PEE, parallel elastic element), and a tendon (SEE, serial elastic element) (A, B). Each point mass is accelerated by its adjacent components, either muscle actuators ($F_i(t)$) or tendon force ($F_{\mathrm{t}}(t)$) (A). The muscle force was the sum of forces from CE and PEE which depended on normalized activation level, normalized muscle force-length property (C, left), and normalized muscle force-velocity property (C, middle). The tendon force from SEE depended on tendon force-length property (C, right). $\hat{F}_{\mathrm{t}}(\hat{l}_{\mathrm{t}})$, normalized tendon force as a function of $\hat{l}_{\mathrm{t}}$; $\hat{F}_{\mathrm{a}}(\hat{l})$, normalized active muscle force as a function of $\hat{l}$; $\hat{F}_{\mathrm{p}}(\hat{l})$, normalized passive muscle force as a function of $\hat{l}$; $\hat{F}_{\mathrm{a}}(\hat{v})$, normalized active muscle force as a function of $\hat{v}$.

Utilizing the time-varying MTU length and muscle activation level obtained from the experiment, along with the computed optimal muscle and slack tendon lengths discussed in Chapter 2, muscle force can be calculated by solving the following equations:

$$F(t) = F_0 \cdot \left(\hat{a}(t)\hat{F}_{\mathrm{a}}\left(\hat{l}(t)\right)\hat{F}_{\mathrm{a}}\left(\frac{d\hat{l}(t)}{dt} \cdot \frac{1}{v_0}\right) + \hat{F}_{\mathrm{p}}\left(\hat{l}(t)\right) \right) \tag{3.1}$$

$$F_{\mathrm{t}}(t) = F_0 \cdot \hat{F}_{\mathrm{t}}\left(\hat{l}_{\mathrm{t}}(t)\right) \tag{3.2}$$

$$F(t) = F_{\mathrm{t}}(t) \tag{3.3}$$

where $\hat{l}(t)$ and $\hat{l}_{\mathrm{t}}(t)$ are normalized muscle belly and tendon lengths, respectively, and F_0 is the maximum isometric muscle force.

The mass-enhanced Hill-type muscle model incorporated muscle mass using 16 point masses distributed along the muscle's length (Figure 3.1A). These masses were connected by Hill-type actuators that generated force to accelerate them. The segments between point masses were modelled using the same formulation as the massless Hill-type model. The last point mass at the free end of the muscle was connected to a massless tendon. Each point mass was accelerated by the resultant of its adjacent forces ($F_{i+1}(t)$, $F_i(t)$, or $F_{\mathrm{t}}(t)$), which changed the position of each point mass ($x_i(t)$). For each point mass, the resultant of the forces from the neighboring segments ($F_{i+1}(t)$ and $F_i(t)$) equaled to the product of mass (m_i) and its acceleration caused by that resultant force. For the last point mass (m_n), the resultant force acting on it came from the force of the n^{th} segment ($F_n(t)$) and the tendon force ($F_{\mathrm{t}}(t)$):

$$F_{i+1}(t) - F_i(t) = m_i \frac{d^2 x_i(t)}{dt^2} \tag{3.4}$$

$$F_{\mathrm{t}}(t) - F_n(t) = m_n \frac{d^2 x_n(t)}{dt^2} \tag{3.5}$$

where i is an integer ranging from 1 to 15, denoting the point mass and segment number, while n is 16, representing the last point mass and segment.

3.3.3. Experimental data processing

The EMG signals of each muscle were transformed into total EMG intensity (a function of the square of EMG signals) using a wavelet decomposition analysis (von Tscharner, 2000) across frequency bands ranging from 10 to 450 Hz. Given the linear relationship between muscle force and EMG signal amplitude (Milner-Brown & Stein, 1975), the square root of the total EMG intensity was used as the measure for muscle excitation (rather than total EMG intensity). Subsequently, muscle excitation ($\hat{u}(t)$) was

normalized to the maximum excitation observed during the 'maximal effort' cycling trials, and then transformed into normalized muscle activation levels ($\hat{a}(t)$) through the application of a transfer function (Zajac, 1989).

$$\frac{d\hat{a}(t)}{dt} + \frac{\hat{a}(t)}{\tau_{\text{act}}} \cdot \left(\beta + \hat{u}(t) \cdot (1-\beta)\right) = \frac{\hat{u}(t)}{\tau_{\text{act}}} \tag{3.6}$$

where β= 0.6 and τ_{act}= 0.045. Details for this process have been described elsewhere (Lee et al., 2011; Dick et al. 2017).

The subject-specific LED maker locations were imported to OpenSim 3.3 (Delp et al., 2007) to scale an existing musculoskeletal model (Rajagopal et al., 2016) and simulate experimentally-matched 3D kinematics. The time-varying muscle-tendon unit (MTU) lengths ($l_{\text{MTU}}(t)$) during each task were estimated using Inverse Kinematics tool. The optimal muscle-tendon unit (MTU) length was calculated as the product of optimal fibre length and the cosine of the pennation angle, plus the slack tendon length, which were provided by a musculoskeletal simulation environment (OpenSim 3.3). The optimal muscle and tendon slack lengths were determined by solving the equation where the passive force produced by the relaxed, static muscle was equivalent to that produced by tendon. These lengths were used to normalize muscle and tendon lengths. Additionally, an initial relaxed, static condition without muscle excitation and MTU length change was created and appended prior to the actual experimental data to facilitate computation as described in Chapter 2.

To test the mass effects, simulations were conducted for comparing muscles of varying masses while maintaining identical musculoskeletal geometric properties. Muscle sizes (masses) were manipulated by multiplying the MTU lengths with twelve different scaling factors, s (s = 0.1, 0.2, 0.5, 1, 1.6, 2, 3, 4, 5, 6, 7, and 10). Consequently, the muscle and tendon lengths were proportional to the scaling factor; the muscle PCSA ($PCSA_0$) and maximum isometric muscle force (F_0) were both proportional to the square of the scaling factor, as F_0 is the product of $PCSA_0$ and maximum isometric stress; the muscle volume, mass, power and work output were proportional to the cube of the scaling factor.

3.3.4. Data analysis

The predicted muscle performances ($\hat{F}$, normalized muscle force; P_v, volume-specific power; W_v volume-specific work done per cycle) predicted by these mass-enhanced and massless Hill-type muscle models were compared for the 20 participants across twelve scaled sizes, four muscles, and three cycling conditions (low cadence-low torque: 80 r.p.m. and 14 N m; low cadence-high torque: 80 r.p.m. and 44 N m; high cadence-low torque: 140 r.p.m. and 13 N m). The muscle power was determined by multiplying instantaneous force and velocity, while net, positive, and negative work done per cycle were computed by integrating mechanical power over time across a crank cycle. Volume-specific power and volume-specific work per cycle were calculated by dividing power and work by the muscle's volume, respectively. The normalized muscle force and volume-specific power were presented as the percentage of the maximum normalized muscle force (% $\hat{F}_0$, where $\hat{F}_0$ equals 1) and the percentage of the optimal volume-specific power ($P_{v,0}$). $P_{v,0}$ was calculated as the product of the maximum area under normalized force-velocity relationship curve during muscle shortening, the maximum isometric muscle stress (σ_0), and the maximum unloaded muscle shortening velocity (v_0). Average values were computed based on data from the last three crank cycles of the testing period.

To compare both model-predicted normalized muscle forces ($\hat{F}$) across scaled sizes, we used the normalized force predicted by the massless model at scale 1 as a reference value. Then, we compared the predicted normalized muscle forces of both the massless and mass-enhanced models across different scales with this reference. The primary outcome measure for assessing the disparity between predicted normalized force and the reference was the root-mean-squared error (RMSE). $RMSE_{ME}$ reflects the difference between the predicted normalized muscle force using the mass-enhanced model at a specific scale and the reference, while $RMSE_{ML}$ indicates the difference for the massless model. The same proves was applied for the evaluation of RMSE in volume-specific power (P_v). Subsequently, a general linear model ANOVA was conducted to explore potential variations in RMSE (dependent variable) considering models, muscles, cycling, and pedaling conditions (fixed variables), along with subjects (random variable). Statistical significance was established at $P<0.05$, and data were presented as means with standard error of the mean (SEM).

To assess the impact of cycling cadence and load on the differences in model-predicted forces, we further examined forces predicted under two additional pedaling conditions: 100 r.p.m. with 14 N m, and 80 r.p.m. with 26 N m. The choice of the VL muscle for analysis was based on its larger volume proportion within a singular lower limb compared to the other three tested muscles (Handsfield et al., 2014), and its substantial contribution to positive work during cycling (Broker and Gregor, 1994; Martin and Brown, 2009). These characteristics enhanced our ability to observe potential mass effects on work more distinctly.

To explore the impact of mass effects on work output, we evaluated the volume-specific MTU work output per cycle (W_v), contrasting predictions from the mass-enhanced model against those from the massless model across varied muscle sizes. Our focus was on the VL and SOL muscles due to their larger volume proportions within the quadriceps and calf muscles, respectively, in comparison to the other muscles studied. These muscles were expected to demonstrate more noticeable mass effects. Additionally, we deliberately opted for a high load (44 Nm) and low cadence (80 rpm) pedalling condition. Previous findings suggested that cycling at higher crank loads and lower cadences tends to yield greater net work output (Lai et al., 2021). This choice aimed to enhance our ability to observe changes in net work output relative to the scale factor.

3.4. Results

When comparing the predicted $\hat{F}$ of the massless model at various scales with that of the massless model at scale 1, our results for high cadence (140 r.p.m.)-low torque (13 N m) condition showed that all the $RMSE_{ML}$ were minimal, with the largest $RMSE_{ML}$ of 0.002 ± 0.000 % $\hat{F}_0$. This suggested that when employing the massless model, the predicted $\hat{F}$ showed minimal changes with the scaled size, staying nearly identical to the predicted $\hat{F}$ at scale 1 (Figure 3.2A). In contrast, the $RMSE_{ME}$ grew exponentially with the scale factor for all tested muscles. When averaged across muscles and subjects, post hoc analysis revealed that the $RMSE_{ME}$ values at scale factors 3 and larger were significantly different from the $RMSE_{ME}$ values at any scale factor, with the largest $RMSE_{ME}$ of 7.043 ± 0.283 % $\hat{F}_0$ at scale 10. No significant differences in $RMSE_{ME}$ were shown among the scale factors 0.1, 0.2, 0.5, 1.0, 1.6, and 2.0, where $RMSE_{ME}$ increased from 0.072 ± 0.041 to 0.441 ± 0.038 % $\hat{F}_0$. This suggested that the discrepancy in the predicted $\hat{F}$, when

considering the mass effect in the model compared to not considering it, became more noticeable with larger muscle sizes. The exponential increase of $RMSE_{ME}$ with scaled muscle sizes was also observed when comparing the volume-specific power (P_v) predicted by the two models across pedalling conditions and muscles (Figure 3.2C).

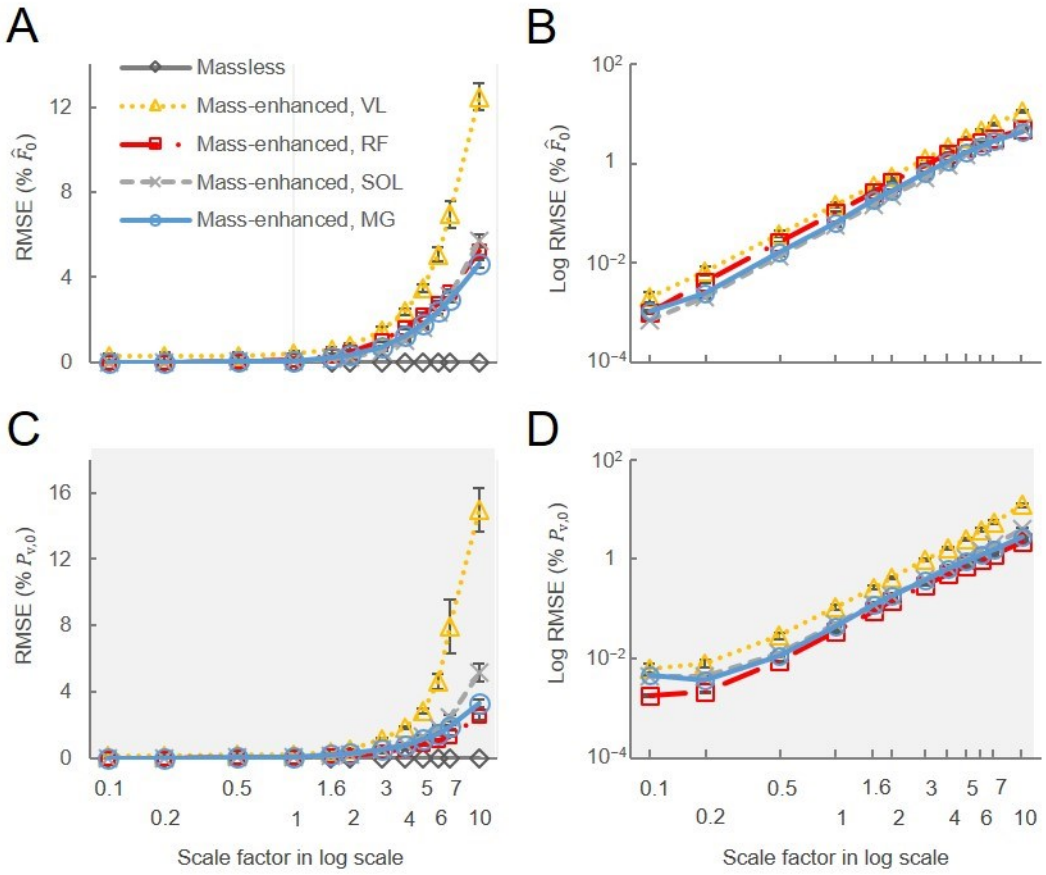

Figure 3.2. The muscle mass (size) effect on the differences between massless and mass-enhanced model predictions of muscle performances.

The diamond marks, linked by a solid dark grey line, illustrate the root-mean-squared error (RMSE) in the normalized muscle forces ($\hat{F}$; A) and the volume-specific power (P_v; C) between the predictions by the massless model at a particular scale and those observed at scale 1 for VL muscle ($RMSE_{ML}$). Other muscle values are not shown due to overlap with VL muscle data. Each additional mark represents the RMSE between the predicted $\hat{F}$ of the mass-enhanced model at a particular scale and that of the massless model at scale 1 ($RMSE_{ME}$). Each distinct colour and shape corresponds to a specific muscle. The X-axis markers have been adjusted to a log scale. (A) $RMSE_{ML}$ is nearly zero across scales, indicating that $\hat{F}$ predicted by the massless model at various scales are almost identical to the $\hat{F}$ predicted at scale 1. In contrast, $RMSE_{ME}$ increases as the scale factor increases across all tested muscles, indicating that $\hat{F}$ predicted by mass-enhanced model deviate more distinctly from the $\hat{F}$ predicted by massless model at scale 1 when muscle size becomes larger. (B) The Y-axis markers have been adjusted to illustrate the log-transformed $RMSE_{ME}$ (Log RMSE). Our results showed a strong linear relationship between the logarithmic values of scale factor and the logarithmic values of $RMSE_{ME}$ across muscles. (C) $RMSE_{ME}$ in P_v also increases as the scale factor increases across all tested muscles. (D) The log-transformed $RMSE_{ME}$ values in P_v shows a linear increase with logarithmic value of scale factor except at scale

0.1. The representative data was taken from muscles in high cadence (140 r.p.m.)-low load (13 N m) pedalling condition averaged across subjects.

As the variance of $RMSE_{ME}$ values across different scales increased with scale factor, it violated one of the assumptions of ANOVA test that requires homogeneous variance among groups. To illustrate the change in $RMSE_{ME}$ across different scale factors, particularly at lower scales, we conducted a logarithmic transformation of the $RMSE_{ME}$ values (Figure 3.2B & 3.2D). We found significant differences in the log-transformed RMSE values in $\hat{F}$ among scale factors (P<0.001), with the differences increasing at larger scale factors. Strong linear relationships were found between the logarithmic values of scale factor and the logarithmic values of $RMSE_{ME}$ in $\hat{F}$ for all muscles (r^2> 0.99). The linear relationship in $\hat{F}$ when averaged across muscles and subjects for high cadence-low torque condition was: $\log(RMSE_{ME}) = 1.9253 \cdot \log(\text{scale factor}) - 1.0566$ (r^2= 0.999), which can be converted as: $RMSE_{ME} = 0.088 \cdot (\text{scale factor})^{1.9253}$. In contrast, the log-transformed RMSE values in P_v, when averaged across muscles, also showed an increase with the scale factor, but no significant differences were found between scales 0.1 and 0.2.

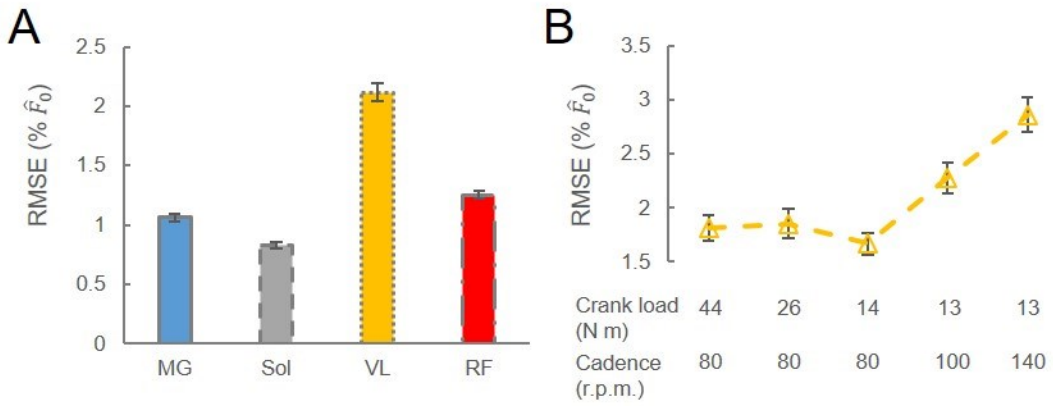

Figure 3.3. Comparison of mass effects among muscles and among pedalling conditions.

(A) The $RMSE_{ME}$ values, when averaged across scales and pedalling conditions, are significantly different among muscles. (B) The $RMSE_{ME}$ values in VL muscle, when averaged across scales, increases significantly with pedalling cadences, with the lowest $RMSE_{ME}$ of 1.666±0.106 % $\hat{F}_0$ for 80 r.p.m., and the highest $RMSE_{ME}$ of 2.866±0.159 % $\hat{F}_0$ for 140 r.p.m.. The $RMSE_{ME}$ values in VL muscle are not significantly different among various crank loads.

We compared the $RMSE_{ME}$ in $\hat{F}$ across tested muscles to analyze the mass effect on model-predicted forces for different muscles during cycling. We found that, when averaged across scales and pedaling conditions, higher $RMSE_{ME}$ values were observed

in the quadriceps muscles (VL, RF) compared to the calf muscles (MG, SOL) (P<0.001). Post hoc analysis revealed significant differences in $RMSE_{ME}$ among muscles (P<0.05). The $RMSE_{ME}$ values for VL, RF, SOL and MG muscles were 2.116±0.076, 1.253±0.034, 0.827±0.030, 1.061±0.032 % $\hat{F}_0$, respectively (Figure 3.3A). This pattern, larger $RMSE_{ME}$ in the quadriceps (VL, RF) compared to the calf muscles (MG, SOL), persisted consistently across all examined scales except scale 0.1. For the comparison of $RMSE_{ME}$ in $\hat{F}$ across various cadences (80-140 r.p.m.) and crank loads (14-44 N m) in VL muscle, our results showed an increase in $RMSE_{ME}$ with higher cycling cadence when the load was set at 13-14 N m (Figure 3.3B). When averaged across scales, the $RMSE_{ME}$ values in VL muscle were 1.666±0.106, 2.274±0.145, 2.866±0.159 % $\hat{F}_0$, for 80, 100, 140 r.p.m., respectively. Significant differences were found among these $RMSE_{ME}$ of different cadences by post hoc analysis (P<0.05). In contrast, when comparing $RMSE_{ME}$ across different crank loads in conditions of fixed cadence (80 r.p.m.), crank loads did not exhibit significant effect on the $RMSE_{ME}$ values. Consequently, the variations between the predictions of the two models increased with the pedaling cadence but showed no significant influence from the crank load factor. This suggested a more pronounced mass effect at higher cadences.

When comparing the $RMSE_{ME}$ values in $\hat{F}$ among the three cadences across scale factors in VL muscle, we found that the $RMSE_{ME}$ values for all three cadences exhibited an exponential increase with the scale factor. Additionally, the higher cadence group consistently showed higher $RMSE_{ME}$ values across scale factors, except at scale 10, where the $RMSE_{ME}$ values for 100 r.p.m. is the highest but not significantly different from those for 140 r.p.m. (Figure 3.4A). When conducting paired comparison between cadences at each scale, the $RMSE_{ME}$ values for 140 r.p.m. became significantly different from those for 80 r.p.m. at scale 3 and larger, while the $RMSE_{ME}$ values for 140 r.p.m. significantly differed from those for 100 r.p.m. at scale 4 and larger. Significant differences in the $RMSE_{ME}$ values between 100 r.p.m. and 80 r.pm. were observed at scale 6 and larger. The log-transformed $RMSE_{ME}$ revealed significant differences among the three cadences across all the scales, showing higher values at higher cadences (Figure 3.4B). However, no significant differences were observed between 80 and 100 r.p.m. at scale 0.1, as well as between 100 and 140 r.p.m. at scales 7 and 10. By examining the linear relationships between log-transformed values of $RMSE_{ME}$ in VL muscle and logarithmic values of scale factor for these three cadences, we found the relationships as: $RMSE_{ME}$ =

$0.068 \cdot (\text{scale factor})^{2.027}$ for 80 r.p.m.; $RMSE_{ME} = 0.088 \cdot (\text{scale factor})^{2.052}$ for 100 r.p.m.; $RMSE_{ME} = 0.150 \cdot (\text{scale factor})^{1.902}$ for 140 r.p.m.. In contrast, the $RMSE_{ME}$ values in $\hat{F}$ across scale factors were not sensitive to crank load across scaled VL muscle sizes (Figure 3.4C & 3.4D). No significant differences in log-transformed RMSE values were found among the three crank load conditions across scales, except for the comparison between crank loads of 14 N m and 26 N m at scale 0.1.

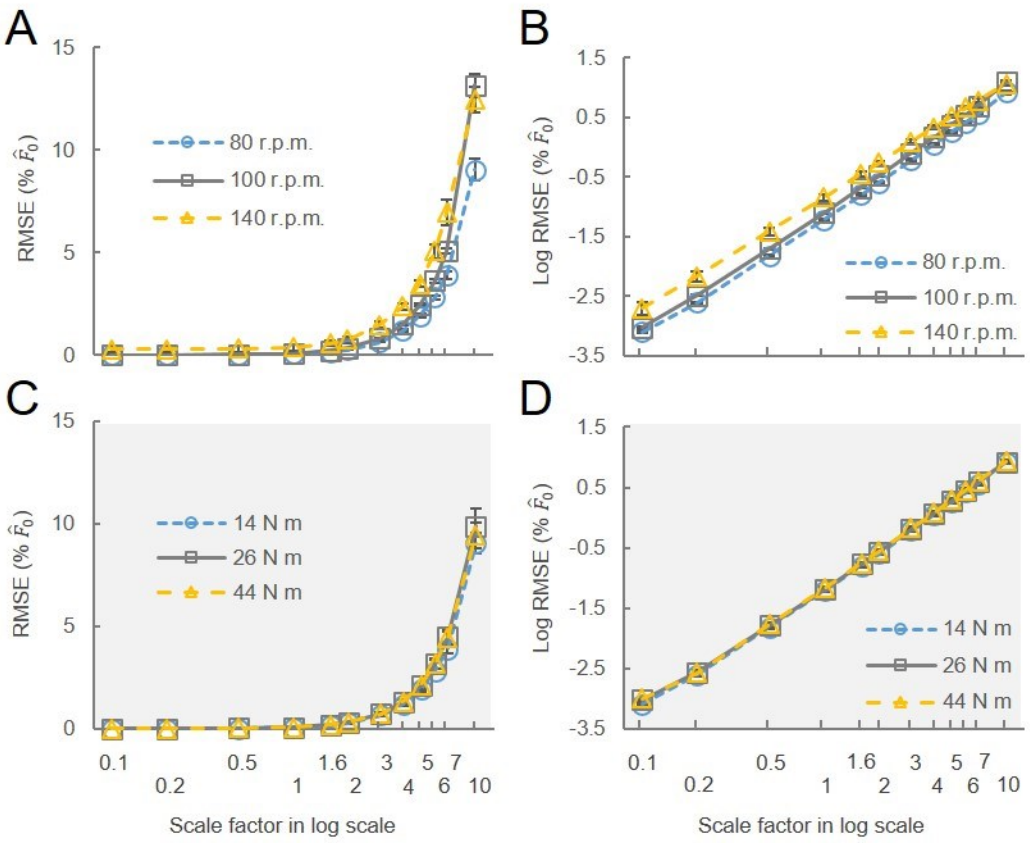

Figure 3.4. The effects of cadence and crank load across various scaled muscle sizes on the differences between the two model-predicted normalized forces.

The X-axis markers have been adjusted to a log scale. (A) The $RMSE_{ME}$ values across scales for different pedalling cadences in VL muscle exhibit an exponential increase with scale factor, with the trend of higher $RMSE_{ME}$ at higher cadence, except at scale 10, where the $RMSE_{ME}$ values for 100 r.p.m. is the highest but not significantly different from those for 140 r.p.m.. (B) Higher cadence groups show higher log-transformed $RMSE_{ME}$ values across scales except at scale 10. (C) $RMSE_{ME}$ for different pedalling crank loads in VL muscle are similar across scales. (D) No significant differences in log-transformed RMSE values were found among the three crank load conditions across scales, except for the comparison between crank loads of 14 N m and 26 N m at scale 0.1.

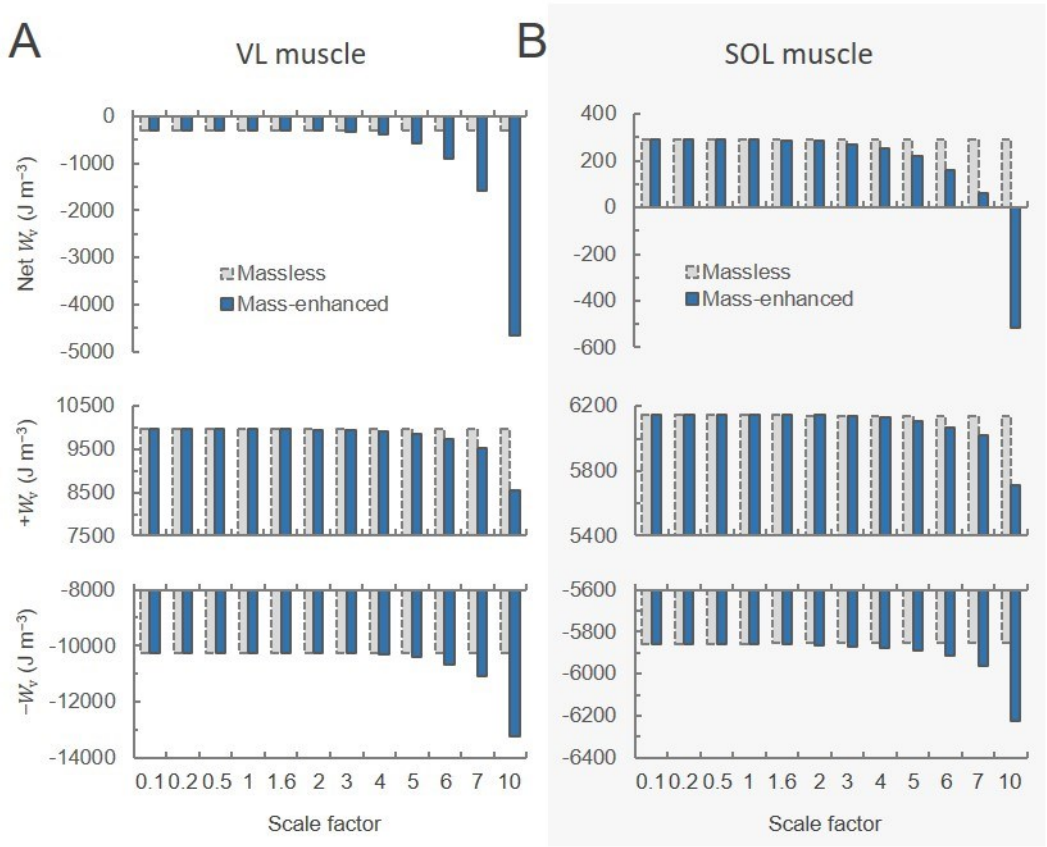

Figure 3.5. Volume-specific MTU work output per cycle (W_v) across scales during high load (44 N m)-low cadence (80 r.p.m.) pedalling condition.

Top, middle, and bottom rows indicate net, positive, negative MTU work output per cycle, respectively, for VL (A) and SOL (B) muscles. Volume-specific MTU work outputs per cycle were predicted using both massless (Grey bar) and mass-enhanced (Dark blue bar) muscle models.

The volume-specific net, positive, and negative MTU work outputs per cycle predicted by the massless model remained relatively constant for both the VL (−288.4, 9962.7, −10251.0 J m^{-3}, respectively) and SOL (290.7, 6149.8, −5859.1 J m^{-3}, respectively) muscles, despite the increasing scale factor (Figure 3.5). In contrast, the volume-specific net, positive, and negative MTU work outputs per cycle predicted by the mass-enhanced model exhibited variability across scales. At smaller scaled sizes (scale factor 1.6 or less), these outputs mirrored those of the massless model, remaining relatively constant. However, beyond a scale factor of 2, there was a noticeable trend: the volume-specific positive work tended to decrease, while there was an increase in the volume-specific negative work. As a result, the volume-specific net work of the MTU tended to become more negative as muscle mass increased. These findings suggested that increased muscle mass led to a reduction in the mechanical work output of the MTU

per cycle as predicted by models incorporating mass effects, in contrast to those without mass considerations.

3.5. Discussions

The study aimed to assess the magnitude of the muscle mass effects in human-sized muscles during higher cadence cyclic movements and the impact of scaled muscle sizes on predicted muscle performances by the mass-enhanced model in comparison to the massless model. Our preliminary investigation (Chapter 2) focusing on activities of daily living displayed minimal mass effects at scale 1, likely due to low muscle acceleration. Hence, the study in this chapter used cycling to achieve a higher cadence (140 r.p.m.) of cyclic movement. Despite this, when assessing mass effects through RMSE between predicted performances using the two models, minimal differences in muscle force and power per cycle (0.158±0.040 % $\hat{F}_0$; 0.094±0.020 % $P_{v,0}$ averaged across muscles) were observed at scale 1. However, upon scaling muscle mass 10^3 times larger, high-cadence cycling showed a larger RMSE value averaged across muscles (7.043 % $\hat{F}_0$) compared to daily activities (4.631 % $\hat{F}_0$ averaged across tasks, with the largest value of 6.272 % $\hat{F}_0$ in hopping). Notably, the increase in RMSE values followed an exponential pattern with the scale factor, suggesting that significant differences in model-predicted forces became apparent only when muscle size reached a certain threshold, indicating the emergence of non-negligible mass effects. Similar findings were reported in previous studies examining scale 10 and 100 on a simulated fibre bundle and rat plantaris muscles, where minimal differences were found between the smaller scale simulations (Ross et al., 2018; Ross et al., 2021). According to the current study, if we consider acceptable errors to be less than 5 %, mass effects might be negligible for a muscle less than 5^3 times larger in mass during 140 r.p.m. cycling; however, it becomes important to consider these effects when dealing with muscles 6^3 times larger in mass or more.

3.5.1. Mass effects in different muscle groups

The quadriceps muscles consistently exhibited larger RMSE values compared to the calf muscles across various pedalling conditions and scales examined in this study. These differences indicate the different magnitude of mass effects between the muscle groups. Given that mass effects depend on the magnitude of tissue mass and its

acceleration, the higher RMSE values in the quadriceps might not only stem from their greater mass but also greater accelerated motion compared to the calf muscles. This aligns with a prior study suggesting that muscles undergoing greater strain movements tend to induce more pronounced mass effects (Ross et al., 2020). Therefore, we compared the root-mean-squared (RMS) MTU strain and acceleration per cycle among these muscles, averaged across subjects and the three cycling conditions. The root-mean-squared (RMS) MTU strain per cycle was 0.074±0.001, 0.038±0.001, 0.049±0.004, and 0.036±0.001 for VL, RF, SOL, and MG muscles, respectively. The RMS MTU acceleration per cycle at scale 1 was 2.165±0.070, 1.355±0.038, 1.411±0.053, 1.461±0.042 m s^{-2} for VL, RF, SOL, and MG muscles, respectively. Additionally, the proportion of muscle volume relative to the total volume of muscles in a single leg is assumed to be 0.1166, 0.0379, 0.0621, and 0.0362 for VL, RF, SOL, and MG muscles, respectively (Handsfield et al., 2014). The VL and SOL muscles occupy a larger proportion of the lower limb volume compared to the RF and MG muscles. The VL muscle had the highest RMS strain and acceleration as well as the largest muscle volume compared to other tested muscles. This might explain why VL muscle exhibited the largest difference in predicted $\hat{F}$ between massless and mass-enhanced models. However, the RF muscle, which exhibited the second largest RMSE in predicted $\hat{F}$, had relatively smaller MTU strain, acceleration and muscle mass. In contrast, the SOL muscle, which had the second highest MTU strain and acceleration as well as the second largest muscle volume, exhibited the lowest RMSE among these muscles in our results (Figure. 3.3A). These findings cannot be attributed to the effects of MTU strain and acceleration on the RMSE values of muscles. In our previous study (Chapter 2), we observed that daily activities with higher MTU acceleration averaged across muscles displayed larger RMSE values (Figure 2.9). However, when we compared the MTU acceleration of each muscle during the same activity, we were unable to identify a clear relationship between a muscle's RMSE values, its MTU acceleration, and muscle mass. Consequently, further investigation is necessary to identify factors influencing the differences in predicted forces among various muscles.

The predicted normalized muscle forces interact with the level of muscle activation (Equation 3.1), potentially influencing the observed errors. A previous study has demonstrated an increase in errors in traditional massless Hill-type models when estimating in situ cat soleus muscle forces during submaximal contractions compared to maximal contractions (Millard et al., 2013). One of the explanation is that inactive fibres in

submaximal contractions contribute to internal load instead of producing force, thus amplifying the mass effect and causing the errors in massless models. To understand how muscle activation affects RMSE values, we further calculated the difference in $\hat{F}$ predicted by mass-enhanced and massless models using the aforementioned equations. We assumed that muscle forces were entirely transmitted to the tendon, equating muscle forces to tendon forces in both models. By utilizing Equations 3.1 – 3.3, the tendon forces of the massless model ($F_{\mathrm{t}}(t)_{\mathrm{ML}}$) were predicted as follows:

$$F_{\mathrm{t}}(t)_{\mathrm{ML}} = F_0 \cdot \left(\hat{a}(t)\hat{F}_{\mathrm{a}}(\hat{l})\hat{F}_{\mathrm{a}}(\hat{v}) + \hat{F}_{\mathrm{p}}(\hat{l})\right) \cdot \cos\alpha \tag{3.7}$$

To calculate tendon forces ($F_{\mathrm{t}}(t)_{\mathrm{ME}}$) in the mass-enhanced model, we combined Equations 3.4 and 3.5 as follows :

$$F_{\mathrm{t}}(t)_{\mathrm{ME}} - F_1(t) = \sum_{i=1}^{n} m_i \frac{d^2 x_i(t)}{dt^2} \tag{3.8}$$

Subsequently, by substituting $F_1(t)$ (the first muscle segment force) with Equation 3.1, the tendon forces were calculated as follows:

$$F_{\mathrm{t}}(t)_{\mathrm{ME}} = \sum_{i=1}^{n} m_i \frac{d^2 x_i(t)}{dt^2} + F_0 \cdot \left(\hat{a}(t)\hat{F}_{\mathrm{a}}(\hat{l}_1)\hat{F}_{\mathrm{a}}(\hat{v}_1) + \hat{F}_{\mathrm{p}}(\hat{l}_1)\right) \cdot \cos\alpha \tag{3.9}$$

where $\hat{l}_1$ and $\hat{v}_1$ were normalized length and velocity of the first muscle segment.

The values of RMSE between model-predicted normalized muscle forces were therefore determined by the differences between Equations 3.7 and 3.9 as follows:

$$\begin{aligned} &\hat{F}_{\mathrm{t}}(t)_{\mathrm{ME}} - \hat{F}_{\mathrm{t}}(t)_{\mathrm{ML}} \\ &\quad = \frac{1}{F_0}\sum_{i=1}^{n} m_i \frac{d^2 x_i(t)}{dt^2} \\ &\quad + \left(\left(\hat{a}(t)\hat{F}_{\mathrm{a}}(\hat{l}_1)\hat{F}_{\mathrm{a}}(\hat{v}_1) + \hat{F}_{\mathrm{p}}(\hat{l}_1)\right)\right. \\ &\quad \left. - \left(\hat{a}(t)\hat{F}_{\mathrm{a}}(\hat{l})\hat{F}_{\mathrm{a}}(\hat{v}) + \hat{F}_{\mathrm{p}}(\hat{l})\right)\right)\cos\alpha \end{aligned} \tag{3.10}$$

The differences between $\hat{F}_{\mathrm{t}}(t)_{\mathrm{ME}}$ and $\hat{F}_{\mathrm{t}}(t)_{\mathrm{ML}}$ stem from two components. One component is related to $\hat{a}(t)$, $\hat{l}_1$, and $\hat{l}$. Since velocity is the first derivative of length with respect to time, $\hat{v}_1$ and $\hat{v}$ are interconnected with $\hat{l}_1$, and $\hat{l}$, respectively. While $\hat{l}$ is derived

by solving Equations 3.1 – 3.3 and is unaffected by scale factor, $\hat{l}_1$ is solved using Equations 3.4 – 3.5 and is influenced by inertial resistance, thus affected by the scale factor. Note that $\hat{a}(t)$ contributes to both $\hat{l}_1$, and $\hat{l}$ calculations. The other component of the difference involves F_0, m_i, and $x_i(t)$. The point masses m_i scale with scale^3, $x_i(t)$ scale with scale^1, and F_0 scale with scale^2, making this component proportional to scale^2. Consequently, this may explain our findings that $RMSE_{ME}$ is proportional to the range from scale$^{1.9}$ to scale^2. While the muscle activation level contributes to the RMSE values, its influence might be outweighed by other factors within Equation 3.10, such as the magnitude of muscle mass and its acceleration.

3.5.2. Mass effects across Pedalling conditions

The impact of mass effects on muscle behaviour during cyclic contractions can vary significantly depending on task conditions. Higher crank torque increases positive MTU work and motor-like function (Lai et al., 2021), whereas higher pedalling cadence triggers earlier muscle excitation, resulting in increased negative work and a spring-like behavior (Neptune et al., 1997; Wakeling et al., 2006; Neptune and Herzog, 1999; Kautz and Neptune, 2002; Lai et al., 2021). To explore this relationship concerning pedalling conditions, we manipulated the mechanical demands of cycling by independently adjusting crank torque and cadence. These alterations challenged muscles to adapt their function to meet the changing mechanical requirements. Our findings align with prior research (Dick et al., 2017; Wakeling et al., 2021), which observed discrepancies between forces predicted by massless models and measured forces across diverse conditions of cyclic movement. Similarly, we discovered discrepancies between functions predicted by massless and mass-enhanced models that were pronounced at higher cadences and unaffected by crank load (Figure. 3.4). This trend suggests that mass effects amplify when muscle mass experiences faster acceleration.

These increased mass effects at higher cadences become more noticeable as scaled muscle size increases (Ross et al., 2020), especially beyond human-sized muscles (Figure 3.4A). Our results showed that when predicting forces of a muscle 6^3 times larger than its original mass, mass effects could lead to errors exceed 5 % at a pedalling cadence of 140 r.p.m., while remaining below 5 % at lower cadences (Figure 3.4A). However, for smaller muscle sizes, mass effects appeared less sensitive to pedalling cadence.

Equation 3.10, which elucidates the variables influencing RMSE calculations, highlights that the scale factor and pedalling cadence, directly linked to mass and acceleration magnitudes, primarily determine these differences. In contrast, crank load, impacting activation levels (Dick et al., 2016), showed no significant effect on the differences.

It is important to highlight that certain alterations in muscle behavior under varying pedalling conditions are not captured in our one-dimensional, single-element, mass-enhanced model. For instance, increased cadence led to a change in the motor unit recruitment (Dick et al., 2017), and an increase in muscle belly gearing (Wakeling et al., 2011) that are both not considered in this study. Also, the impact of muscle mass in the two-element muscle models (Lee et al., 2013b) and three-dimension muscle models (Ross et al., 2018b) was additionally not considered and warrants further investigation.

3.5.3. Mass effects on volume-specific work across scaled sizes

Research has consistently shown that increased muscle mass correlates with decreased mechanical work output during cyclic movements (Ross et al., 2018; Ross et al., 2020; Ross et al., 2021). As muscles become larger, maintaining similar geometric properties, their force-generating capacity increases with cross-sectional area while their mass increases with volume. Consequently, larger muscles encounter higher inertial loads relative to the force they produce, demanding more internal work to deform muscle tissue and accelerate their internal mass, especially within three-dimensional models (Ross et al., 2021). This inertial cost becomes more pronounced in larger muscles, resulting in reduced external volume-specific work as the finite amount of energy available during contraction is diverted to strain-energy potentials within the tissue and to accelerate internal mass (Wakeling et al., 2020; Ross et al. 2021).

Our results indicate a decrease in net volume-specific work per cycle for the VL and SOL muscles with increased muscle size, consistent with previous findings (Ross et al., 2018b; Ross et al., 2020; Ross et al., 2021). However, a notable disparity was observed in the VL muscle, exhibiting a negative net work output during low cadence-high load cycling. This contradicts earlier research suggesting that the VL is a primary contributor to positive work during cycling (Broker & Gregor, 1994; Lai et al., 2021). To investigate this discrepancy, we compared our study, which utilized the same experimental data as Lai and colleagues (2021), to their methods. In our study, we

employed measured EMG intensity to calculate muscle activation, while Lai and colleagues used computed muscle control (CMC) (Thelen & Anderson, 2006) to predict muscle excitation and activation. Upon examining our experimental VL muscle activation data, we observed inconsistency in VL muscle activation across pedalling cycles among subjects. This might introduce potential errors in predicting muscle function. Additionally, while the CMC-predicted activation drops to nearly zero around 270 degrees of the crank cycle, the measured activation remains non-zero, suggesting that the VL muscle is activated and undergoes eccentric contraction during this recovery phase of cycling. This discrepancy may contribute to a greater negative power and work output in our study compared to using CMC-predicted activation.

The reduction in mechanical work output per cycle due to increased muscle mass varied among studies, potentially attributable to differences in the muscles studied and experimental conditions. Ross and colleagues (2018) simulated muscle contractions using a fibre-bundle sized muscle (6.7×10^{-7} kg), observing a 12% reduction in mechanical work with a 100^3-fold increase in muscle mass. In another study on rat plantaris muscles (5.71×10^{-4} kg), a 123% increase in effective mass led to a 4.7% reduction in mechanical work (Ross et al., 2020). When simulating the contraction of the rat plantaris muscle with muscle strain set at 10 %, an approximately 10% reduction in work was observed by adding about 250% lumped effective mass, whereas an approximately 10 % reduction in work was observed by adding about 375% distributed effective mass (Ross et al., 2020). However, our focus on human muscles, notably larger, led us to observe a 9.4 % reduction in predicted MTU net work per cycle for the VL muscle (0.870 kg averaged across subjects) scaled up to 3^3 times their original size during high load-low cadence pedalling, and a 12.6 % reduction for the SOL muscle (0.463 kg) scaled up to 4^3 times their original size (Figure 3.5). Additionally, our study explored evenly distributed muscle mass along the muscle length. Unlike concentrating mass in specific positions, distributed mass showed reduced mass effects with increased muscle mass (Ross et al., 2020). This is because distributed point masses, which can move independently, have the potential to reduce overall resistance to force generation due to opposite directions of inertial resistance, thereby mitigating the mass effects. Although distributed mass simulations might better model continuous mass throughout a muscle volume, real muscles typically exhibit uneven volume or mass distribution along their length. For instance, human leg muscles have their greatest cross-sectional area at the midpoint, gradually tapering off towards both proximal

and distal ends (Fukunaga et al., 1992; Maden-Wilkinson et al., 2013). Also, regional variations in muscle activation could affect the distribution of inactive muscle mass during submaximal contractions (Wakeling, 2009; Hodson-Tole et al., 2013). Therefore, neither lumped nor distributed muscle mass could fully capture the complex inertial properties of *in vivo* muscles.

Furthermore, our study incorporates models featuring a tendon in series. The impact of the tendon on overall muscle-tendon unit (MTU) work depends on the phase of excitation relative to the initiation of MTU shortening (Lichtwark et al., 2005; Ettema, 1996; Ettema, 2001; Sawicki et al., 2015). Early muscle activation during MTU lengthening can facilitate the storage of elastic energy within the tendon, capable of preserving energy from external work and the contraction of muscle fibers (Ettema, 2001). This stored elastic energy can subsequently be utilized during the shortening phase, enhancing both MTU work output and efficiency. However, in our study, because of the identical activations relative to the MTU shorten-lengthening cycle, regardless of scaled size, the interplay between the excitation phase and MTU stretch-shortening cycle remained consistent across models and scale factors. With the inclusion of mass in the model, scaled across different sizes, it influences both muscle and tendon length alterations while maintaining a constant MTU shorten-lengthening cycle. The inertial resistance might result in the uncoupling of muscle length changes from MTU length changes, causing the tendon to shorten while the MTU elongates. Consequently, this may limit or prevent energy storage within the tendon, leading to a decrease or absence of external work. The variance in tendon effects across scaled masses is reliant on the relative alterations in tendon length caused by inertial resistance.

3.6. Conclusions

This study provided insights into the effects of muscle mass on performances during high-cadence movements in humans. Our results suggested that, while normalized forces predicted by a massless model remained constant across scaled muscle sizes, the differences between the normalized forces predicted by mass-enhanced models and those by the massless model increased exponentially with scaled muscle sizes, indicating a greater impact of mass in larger muscles. The vastus lateralis muscle exhibited a greater mass effect compared to other muscles, possibly due to its larger size, greater MTU strain and acceleration during cycling. Additionally, greater mass effects were observed at higher

cycling cadences where the accelerations were high, while crank load did not influence these effects. Furthermore, volume-specific net work output per cycle decreased as muscle mass increased. In conclusion, muscle mass is a crucial determinant of skeletal muscle behavior, particularly in muscles larger than human-sized muscles and particularly during high-cadence movement.

Chapter 4.

Mass effects on human muscle function: implications, limitations, and future directions

4.1. Summary of thesis

Muscle mass has been considered as a crucial determinant influencing overall muscle contractile behavior throughout the body. Previous studies exploring the impact of mass on muscle performance reveal significant outcomes: greater muscle mass is associated with a reduction in the rate of muscle force development (Günther et al., 2012), a decrease in maximum contraction velocity (Meier & Blickhan, 2000; Böl & Reese, 2008; Ross & Wakeling, 2016), lowered mass-specific mechanical work output, and average power per cycle (Ross et al., 2018a; Ross et al., 2020). Efficiency of muscle contraction is also diminished with increased muscle mass (Ross & Wakeling, 2021). Moreover, three-dimensional models, accounting for muscle mass, highlight that greater muscle mass leads to heightened volume-specific internal kinetic energy, increased energy stored in the aponeurosis, and non-uniform tissue acceleration during contractions (Ross & Wakeling, 2021). Despite these findings, examinations of mass effects and models integrating these effects had been primarily confined to in silico and in situ experiments. Notably, there was a lack of research investigating the effects of muscle mass in living human muscles during locomotion— a scenario where muscles undergo submaximal contraction and cyclic movement, with tissue mass likely exerting a substantial impact.

In my first study (Chapter 2), I used a mass-enhanced Hill-type muscle model to simulate human muscle contractions during various daily activities. I compared the predicted forces with those of a more traditional massless Hill-type model across scaled muscle mass, different muscles, and varied tasks. The assessment of the root-mean-squared errors (RMSE) between the two model-predicted forces served as an indicator of the impact of muscle mass, where a larger RMSE denoted more substantial mass effects. The findings indicated that while mass effects can significantly influence muscle performance in daily human movement, their impact is minimal and perhaps negligible in human-sized or smaller muscles. However, this effect becomes more pronounced as muscles scale to larger sizes. Moreover, the study revealed that mass effects were

particularly prominent during running and hopping compared to walking and sit-to-stand tasks across all tested muscles and scaled sizes. Specifically, the quadriceps (vastus lateralis and rectus femoris) exhibited greater mass effects compared to calf muscles (medial gastrocnemius and soleus) at original or larger scaled sizes across all tasks, except in hopping where soleus muscle displayed the most significant mass effects. Notably, the disparities between tasks or among muscle groups were more prominent at larger scaled muscle sizes. These variations might be attributed to differences in each muscle's mass and its accelerations, with greater mass effects observed in muscles with larger mass and higher acceleration during higher-cadence movement tasks.

The limited mass effects observed in human-sized muscles during daily activities in Chapter 2, potentially due to the relatively low acceleration of muscle mass in these scenarios, prompted the exploration of more pronounced mass effects in my second study (Chapter 3). In this study, cycling was employed, offering the opportunity to increase the cadence of movement while keeping kinematics constant. This approach aimed to assess whether mass effects could become more prominent and to analyze the variations in mass effects across scaled sizes and pedaling conditions. The findings revealed that the effects of muscle mass, evaluated through the RMSE between the two model-predicted forces, exhibited an exponential increase with the scale factor, featuring an exponent of around 2. Notably, the RMSE surpassed 5 % when muscle mass was 6^3 times larger or more, depending on specific muscles and pedaling conditions. Furthermore, consistent observations indicated larger RMSE and consequently greater mass effects in the quadriceps compared to the calf muscles across all examined scales. Additionally, the study unveiled that mass effects increased with pedaling cadence, while exhibiting no significant influence from the crank load factor. Moreover, greater muscle mass resulted in a reduction in mechanical work output per cycle, as predicted by mass-enhanced models, in contrast to massless models. In summary, the studies within this thesis contribute valuable insights into the extent of muscle mass effects on contractile performances across various types of human locomotion.

4.2. Limitations and future directions

This is the first study exploring mass effects on muscle performances during human locomotion. Although the study has broadened our initial understanding of the extent of muscle mass effects across various scaled muscle sizes and activities by

examining the prediction disparities between mass-enhanced and massless models, it is imperative to acknowledge certain limitations in the current model employed in this study. These limitations stem from certain assumptions and constraints, preventing the model from fully capturing the diverse spectrum of potential muscle properties and contraction conditions inherent in real muscles.

Firstly, while the outcomes of my studies shed light on potential errors in predicting forces using a massless model, they fall short of providing insights into the accuracy of predicting forces using mass-enhanced models or the degree of similarity between predicted and measured forces. In subsequent research, it would be beneficial to explore avenues such as comparing predicted forces from mass-enhanced models to ultrasound-measured forces in human muscles during cycling (Dick et al., 2017). Additionally, comparing predicted forces to directly measured forces in animal muscles could offer further insights into the accuracy of mass-enhanced models.

Secondly, the varied functions of each muscle in different movement tasks and conditions are influenced by factors such as unique kinematics, the timing of muscle activation and the resultant force in relation to muscle strain (Biewener et al., 2004; Dickinson et al., 2000; Josephson, 1985; Roberts et al., 1997), and the number of joints the muscle crosses (Zajac & Gordon, 1989 ; Prilutsky, 2000). For example, increased hip and knee flexion, along with higher electromyographic activity were observed in quadriceps and hamstrings during running as compared to walking (Mann & Hagy, 1980). Muscles, undergoing eccentric contractions in walking, may transition to concentric contractions during the initial floor contact in running (Mann & Hagy, 1980). Furthermore, muscles can exhibit various behaviours, acting as motors (generate positive work), springs (store and recover elastic strain energy), struts (generate force with minimal length change), or dampers (lengthen to absorb energy), depending on factors like external environment and intrinsic muscle properties (Dickinson et al., 2000; Biewener, 2016). Examples include the proximal-distal gradient of lower-limb muscle organization, with distal muscles exhibiting more strut-like behaviours favoring force development and spring-like storage of elastic energy in humans (Lai et al., 2015), while proximal muscles generally act as motor, producing positive work (Biewener, 1998; Biewener & Daley, 2007). Moreover, during maximal cycling, hip extensor muscles contribute predominantly to positive power generation, while in submaximal cycling, knee extensors and flexors also play a role in generating positive power (Martin and Brown, 2009; Martin and Nichols,

2018; Broker & Gregor, 1994). Greater crank load during cycling results in a more motor-like muscle function, whereas higher pedalling cadence leads to a more spring-like muscle behaviour (Lai et al, 2021). Since the differences in muscle activity and mass acceleration arise from varying mechanical demands across different movement tasks, these variations in muscle activity and mass acceleration contribute to distinct extents of mass effects on muscle functions.

Last but not least, additional factors influencing muscle function were not incorporated into the models presented in my thesis. These factors include fiber-type composition and recruitment patterns, muscle geometries and architectures, and the non-uniform behavior of muscle tissue during contraction. The current one-element model focused on slow fibers in daily activities and fast fibers in cycling. However, studies suggest that two-element models perform better in high-cadence tasks like hopping and running (>100 r.p.m.) (Dick et al., 2017), prompting consideration for developing a two-element model to assess mass effects. Furthermore, the proportion of slow and fast fibers varies among muscles (Edgerton et al., 1975), suggesting the potential benefits of employing muscle-specific models for better predictions. Additionally, the one-dimensional (1D) model in my thesis lacks considerations for muscle shape changes (Hodgson et al., 2006; Baskin & Paolini, 1967) and architectural gearing effects (Azizi et al., 2008), thus overlooking tissue mass effects in other dimensions. Although three-dimensional (3D) models accounting for tissue mass exhibit greater reductions in mass-specific mechanical work output per cycle, a direct comparison of prediction accuracy between 3D and 1D models concerning measured muscle functions requires further investigation. Moreover, within different regions of a whole muscle, fascicles may experience varying strains and accelerations, positioning themselves differently on force-length or force-velocity curves at a given time (Pappas et al., 2002; Ahn et al., 2003; Soman et al., 2005; Shin et al., 2009; Ahn et al., 2018; Ross et al., 2021). This tissue non-uniformity, attributed to variations in activation (Monti et al., 2003; Rahemi et al., 2014), myofascial force transmission (Tijs et al., 2015), and tissue mass (Ross et al., 2021), is not considered in the models presented in my thesis.

In conclusion, advancing the accuracy of predicting actual muscle forces requires further research to develop a comprehensive model. This model should not only consider the diverse effects of influential factors on muscle functions but also enable the customization of factor weights. Factors such as muscle type, size, activity, task conditions,

health status, and species should be incorporated, allowing for an in-depth understanding of complex muscle behaviours. The clinical implications of such a refined model are vast, presenting opportunities for analyzing kinetic and kinematic alterations in neuromuscular disorders (Hicks et al., 2008; Steele et al., 2010), formulating targeted rehabilitation strategies (Hall et al., 2011; Peterson et al., 2011), and influencing the design of various assistive devices (Uchida et al., 2016), prostheses (Grimmer & Seyfarth, 2014), and powered exoskeletons (Federici et al., 2015). These endeavors hold the potential to significantly contribute to our understanding of muscle mechanics across a spectrum of real-world scenarios.

References

Abbott, B. C., & Aubert, X. M. (1952). The force exerted by active striated muscle during and after change of length. The Journal of physiology, 117(1), 77–86.

Ahn, A. N., Monti, R. J., & Biewener, A. A. (2003). In vivo and in vitro heterogeneity of segment length changes in the semimembranosus muscle of the toad. The Journal of physiology, 549(Pt 3), 877–888. https://doi.org/10.1113/jphysiol.2002.038018

Ahn, A. N., Konow, N., Tijs, C., & Biewener, A. A. (2018). Different Segments within Vertebrate Muscles Can Operate on Different Regions of Their Force-Length Relationships. Integrative and comparative biology, 58(2), 219–231. https://doi.org/10.1093/icb/icy040

Andrews, A. W., Thomas, M. W., & Bohannon, R. W. (1996). Normative values for isometric muscle force measurements obtained with hand-held dynamometers. Physical therapy, 76(3), 248–259. https://doi.org/10.1093/ptj/76.3.248

Asakawa, D. S., Pappas, G. P., Blemker, S. S., Drace, J. E., & Delp, S. L. (2003). Cine phase-contrast magnetic resonance imaging as a tool for quantification of skeletal muscle motion. Seminars in musculoskeletal radiology, 7(4), 287–295. https://doi.org/10.1055/s-2004-815676

Azizi, E., Brainerd, E. L., & Roberts, T. J. (2008). Variable gearing in pennate muscles. Proceedings of the National Academy of Sciences of the United States of America, 105(5), 1745–1750. https://doi.org/10.1073/pnas.0709212105

Baskin, R. J., & Paolini, P. J. (1967). Volume change and pressure development in muscle during contraction. The American journal of physiology, 213(4), 1025–1030. https://doi.org/10.1152/ajplegacy.1967.213.4.1025

Best, T. M., McElhaney, J., Garrett, W. E., Jr, & Myers, B. S. (1994). Characterization of the passive responses of live skeletal muscle using the quasi-linear theory of viscoelasticity. Journal of biomechanics, 27(4), 413–419. https://doi.org/10.1016/0021-9290(94)90017-5

Biewener, A. A. (1998). Muscle function in vivo: A comparison of muscles used for elastic energy savings versus muscles used to generate mechanical power. American Zoologist, 38 (4), 703-717.

Biewener, A. A., McGowan, C., Card, G. M., & Baudinette, R. V. (2004). Dynamics of leg muscle function in tammar wallabies (M. eugenii) during level versus incline hopping. The Journal of experimental biology, 207(Pt 2), 211–223. https://doi.org/10.1242/jeb.00764

Biewener, A. A., & Daley, M. A. (2007). Unsteady locomotion: integrating muscle function with whole body dynamics and neuromuscular control. The Journal of experimental biology, 210(Pt 17), 2949–2960. https://doi.org/10.1242/jeb.005801

Biewener A. A. (2016). Locomotion as an emergent property of muscle contractile dynamics. The Journal of experimental biology, 219(Pt 2), 285–294. https://doi.org/10.1242/jeb.123935

Blake, O. M., & Wakeling, J. M. (2014). Early deactivation of slower muscle fibres at high movement frequencies. Journal of Experimental Biology, 217 (19), 3528- 3534.

Blake, O. M., & Wakeling, J. M. (2015). Muscle coordination limits efficiency and power output of human limb movement under a wide range of mechanical demands. Journal of neurophysiology, 114(6), 3283–3295. https://doi.org/10.1152/jn.00765.2015

Baskin, R. J., & Paolini, P. J. (1967). Volume change and pressure development in muscle during contraction. The American journal of physiology, 213(4), 1025–1030. https://doi.org/10.1152/ajplegacy.1967.213.4.1025

Boggs, D. F., & Dial, K. P. (1993). Neuromuscular organization and regional EMG activity of the pectoralis in the pigeon. Journal of morphology, 218(1), 43–57. https://doi.org/10.1002/jmor.1052180104

Böl, M., & Reese, S. (2008). Micromechanical modelling of skeletal muscles based on the finite element method. Computer methods in biomechanics and biomedical engineering, 11(5), 489–504. https://doi.org/10.1080/10255840701771750

Broker, J. P., & Gregor, R. J. (1994). Mechanical energy management in cycling: source relations and energy expenditure. Medicine and science in sports and exercise, 26(1), 64–74.

Cotofana, S., Hudelmaier, M., Wirth, W., Himmer, M., Ring-Dimitriou, S., Sänger, A. M., & Eckstein, F. (2010). Correlation between single-slice muscle anatomical cross-sectional area and muscle volume in thigh extensors, flexors and adductors of perimenopausal women. European journal of applied physiology, 110(1), 91–97. https://doi.org/10.1007/s00421-010-1477-8

Cronin, N. J., & Lichtwark, G. (2013). The use of ultrasound to study muscle–tendon function in human posture and locomotion. Gait & Posture, 37 (3), 305-312.

Cutts, A., Alexander, R. M., & Ker, R. F. (1991). Ratios of cross-sectional areas of muscles and their tendons in a healthy human forearm. Journal of anatomy, 176, 133–137.

Delp, S. L., Anderson, F. C., Arnold, A. S., Loan, P., Habib, A., John, C. T., Guendelman, E., & Thelen, D. G. (2007). OpenSim: open-source software to create and analyze dynamic simulations of movement. IEEE transactions on bio-medical engineering, 54(11), 1940–1950. https://doi.org/10.1109/TBME.2007.901024

Dick, T. J. M., Arnold, A. S., & Wakeling, J. M. (2016). Quantifying Achilles tendon force in vivo from ultrasound images. Journal of biomechanics, 49(14), 3200–3207. https://doi.org/10.1016/j.jbiomech.2016.07.036

Dick, T. J. M., Biewener, A. A., & Wakeling, J. M. (2017). Comparison of human gastrocnemius forces predicted by Hill-type muscle models and estimated from ultrasound images. The Journal of experimental biology, 220(Pt 9), 1643–1653. https://doi.org/10.1242/jeb.154807

Dickinson, M. H., Farley, C. T., Full, R. J., Koehl, M. A., Kram, R., & Lehman, S. (2000). How animals move: an integrative view. Science (New York, N.Y.), 288(5463), 100–106. https://doi.org/10.1126/science.288.5463.100

Edgerton, V. R., Smith, J. L., & Simpson, D. R. (1975). Muscle fibre type populations of human leg muscles. The Histochemical journal, 7(3), 259–266. https://doi.org/10.1007/BF01003594

Edman, K. A., Elzinga, G., & Noble, M. I. (1982). Residual force enhancement after stretch of contracting frog single muscle fibers. The Journal of general physiology, 80(5), 769–784. https://doi.org/10.1085/jgp.80.5.769

English A. W. (1984). An electromyographic analysis of compartments in cat lateral gastrocnemius muscle during unrestrained locomotion. Journal of neurophysiology, 52(1), 114–125. https://doi.org/10.1152/jn.1984.52.1.114

Erskine, R. M., Jones, D. A., Maganaris, C. N., & Degens, H. (2009). In vivo specific tension of the human quadriceps femoris muscle. European journal of applied physiology, 106(6), 827–838. https://doi.org/10.1007/s00421-009-1085-7

Ettema G. J. (1996). Mechanical efficiency and efficiency of storage and release of series elastic energy in skeletal muscle during stretch-shorten cycles. The Journal of experimental biology, 199(Pt 9), 1983–1997. https://doi.org/10.1242/jeb.199.9.1983

Ettema G. J. (2001). Muscle efficiency: the controversial role of elasticity and mechanical energy conversion in stretch-shortening cycles. European journal of applied physiology, 85(5), 457–465. https://doi.org/10.1007/s004210100464

Federici, S., Meloni, F., Bracalenti, M., & De Filippis, M. L. (2015). The effectiveness of powered, active lower limb exoskeletons in neurorehabilitation: A systematic review. NeuroRehabilitation, 37(3), 321–340. https://doi.org/10.3233/NRE-151265

Frontera, W. R., & Ochala, J. (2015). Skeletal muscle: a brief review of structure and function. Calcified tissue international, 96(3), 183–195. https://doi.org/10.1007/s00223-014-9915-y

Fukunaga, T., Roy, R. R., Shellock, F. G., Hodgson, J. A., Day, M. K., Lee, P. L., Kwong-Fu, H., & Edgerton, V. R. (1992). Physiological cross-sectional area of human leg muscles based on magnetic resonance imaging. Journal of orthopaedic research : official publication of the Orthopaedic Research Society, 10(6), 928–934. https://doi.org/10.1002/jor.1100100623

Full, R., & Ahn, A. (1995). Static forces and moments generated in the insect leg: comparison of a three-dimensional musculo-skeletal computer model with experimental measurements. The Journal of experimental biology, 198(Pt 6), 1285–1298. https://doi.org/10.1242/jeb.198.6.1285

Gasser, H. S., & Hill, A. V. (1924). The dynamics of muscular contraction. Proceedings of the Royal Society of London Series B: Biological Sciences, 96 (678), 398-437. doi: 10.1098/rspb.1924.0035

Geremia, J. M. et al. (2018). Effects of high loading by eccentric triceps surae training on Achilles tendon properties in humans. Eur. J. Appl. Physiol. 118, 1725–1736.

Gomes, A. A., Ackermann, M., Ferreira, J. P., Orselli, M. I. V., & Sacco, I. C. N. (2017). Muscle force distribution of the lower limbs during walking in diabetic individuals with and without polyneuropathy. Journal of neuroengineering and rehabilitation, 14(1), 111. https://doi.org/10.1186/s12984-017-0327-x

Grimmer, M., & Seyfarth, A. (2014). Mimicking human-like leg function in prosthetic limbs. In P. Artemiadis (Ed.), Neuro-robotics (p. 105-155). Dordrecht: Springer

Günther, M., Röhrle, O., Haeufle, D. F., & Schmitt, S. (2012). Spreading out muscle mass within a Hill-type model: a computer simulation study. Computational and mathematical methods in medicine, 2012, 848630. https://doi.org/10.1155/2012/848630

Hall, A. L., Peterson, C. L., Kautz, S. A., & Neptune, R. R. (2011). Relationships between muscle contributions to walking subtasks and functional walking status in persons with post-stroke hemiparesis. Clinical biomechanics (Bristol, Avon), 26(5), 509–515. https://doi.org/10.1016/j.clinbiomech.2010.12.010

Handsfield, G. G., Meyer, C. H., Hart, J. M., Abel, M. F., & Blemker, S. S. (2014). Relationships of 35 lower limb muscles to height and body mass quantified using MRI. Journal of biomechanics, 47(3), 631–638. https://doi.org/10.1016/j.jbiomech.2013.12.002

Hatze H. (1977). A myocybernetic control model of skeletal muscle. Biological cybernetics, 25(2), 103–119. https://doi.org/10.1007/BF00337268

Heerkens, Y. F., Woittiez, R. D., Kiela, J., Huijing, P. A., Huson, A., van Ingen Schenau, G. J., & Rozendal, R. H. (1987). Mechanical properties of passive rat muscle during sinusoidal stretching. Pflugers Archiv : European journal of physiology, 409(4-5), 438–447. https://doi.org/10.1007/BF00583799

Herzog, W., Leonard, T., Joumaa, V., DuVall, M., & Panchangam, A. (2012). The three filament model of skeletal muscle stability and force production. Molecular & cellular biomechanics : MCB, 9(3), 175–191.

Herzog, W., & Leonard, T. R. (2000). The history dependence of force production in mammalian skeletal muscle following stretch-shortening and shortening-stretch cycles. Journal of biomechanics, 33(5), 531–542. https://doi.org/10.1016/s0021-9290(99)00221-3

Herzog, W., & Leonard, T. R. (2002). Force enhancement following stretching of skeletal muscle: a new mechanism. The Journal of experimental biology, 205(Pt 9), 1275–1283. https://doi.org/10.1242/jeb.205.9.1275

Hicks, J. L., Schwartz, M. H., Arnold, A. S., & Delp, S. L. (2008). Crouched postures reduce the capacity of muscles to extend the hip and knee during the single-limb stance phase of gait. Journal of biomechanics, 41(5), 960–967. https://doi.org/10.1016/j.jbiomech.2008.01.002

Hill, A.V. (1938) The Heat of Shortening and the Dynamic Constants of Muscle. Proceedings of the Royal Society of London, 126, 136-195. http://dx.doi.org/10.1098/rspb.1938.0050

Hodgson, J. A., Finni, T., Lai, A. M., Edgerton, V. R., & Sinha, S. (2006). Influence of structure on the tissue dynamics of the human soleus muscle observed in mri studies during isometric contractions. Journal of Morphology, 267 (5), 584-601. doi: 10.1002/jmor.10421

Hodson-Tole, E. F., Loram, I. D., & Vieira, T. M. (2013). Myoelectric activity along human gastrocnemius medialis: different spatial distributions of postural and electrically elicited surface potentials. Journal of electromyography and kinesiology : official journal of the International Society of Electrophysiological Kinesiology, 23(1), 43–50. https://doi.org/10.1016/j.jelekin.2012.08.003

Holt, N. C., Wakeling, J. M., & Biewener, A. A. (2014). The effect of fast and slow motor unit activation on whole-muscle mechanical performance: the size principle may not pose a mechanical paradox. Proceedings. Biological sciences, 281(1783), 20140002. https://doi.org/10.1098/rspb.2014.0002

Hull, M. L., & Jorge, M. (1985). A method for biomechanical analysis of bicycle pedalling. Journal of biomechanics, 18(9), 631–644. https://doi.org/10.1016/0021-9290(85)90019-3

Hutchinson, J. R., & Garcia, M. (2002). Tyrannosaurus was not a fast runner. Nature, 415(6875), 1018–1021. https://doi.org/10.1038/4151018a

Janssen, I., Heymsfield, S. B., Wang, Z. M., & Ross, R. (2000). Skeletal muscle mass and distribution in 468 men and women aged 18-88 yr. Journal of applied physiology (Bethesda, Md. : 1985), 89(1), 81–88. https://doi.org/10.1152/jappl.2000.89.1.81

Johnson GA, Tramaglini DM, Levine RE, Ohno K, Choi NY, Woo SL. Tensile and viscoelasticfckLRproperties of human patellar tendon. J Orthop Res, 1994; 12(6): 796–803.

Josephson, R. K., & Edman, K. A. (1988). The consequences of fibre heterogeneity on the force-velocity relation of skeletal muscle. Acta physiologica Scandinavica, 132(3), 341–352. https://doi.org/10.1111/j.1748-1716.1988.tb08338.x

Kargo, W. J., Nelson, F., & Rome, L. C. (2002). Jumping in frogs: assessing the design of the skeletal system by anatomically realistic modeling and forward dynamic simulation. The Journal of experimental biology, 205(Pt 12), 1683–1702. https://doi.org/10.1242/jeb.205.12.1683

Kaufman, K. R., An, K. W., Litchy, W. J., & Chao, E. Y. (1991). Physiological prediction of muscle forces--I. Theoretical formulation. Neuroscience, 40(3), 781–792. https://doi.org/10.1016/0306-4522(91)90012-d

Kinugasa, R., Kawakami, Y., Sinha, S., & Fukunaga, T. (2011). Unique spatial distribution of in vivo human muscle activation. Experimental physiology, 96(9), 938–948. https://doi.org/10.1113/expphysiol.2011.057562

Kovács, B., Kóbor, I., Gyimes, Z. et al. Lower leg muscle–tendon unit characteristics are related to marathon running performance. Sci Rep 10, 17870 (2020). https://doi.org/10.1038/s41598-020-73742-5

Lai, A., Lichtwark, G. A., Schache, A. G., Lin, Y. C., Brown, N. A., & Pandy, M. G. (2015). In vivo behavior of the human soleus muscle with increasing walking and running speeds. Journal of applied physiology (Bethesda, Md. : 1985), 118(10), 1266–1275. https://doi.org/10.1152/japplphysiol.00128.2015

Lai, A. K. M., Dick, T. J. M., Brown, N. A. T., Biewener, A. A., & Wakeling, J. M. (2021). Lower-limb muscle function is influenced by changing mechanical demands in cycling. The Journal of experimental biology, 224(Pt 3), jeb228221. https://doi.org/10.1242/jeb.228221

Lee, S. S., Miara, M.deB., Arnold, A. S., Biewener, A. A., & Wakeling, J. M. (2011). EMG analysis tuned for determining the timing and level of activation in different motor units. Journal of electromyography and kinesiology : official journal of the International Society of Electrophysiological Kinesiology, 21(4), 557–565. https://doi.org/10.1016/j.jelekin.2011.04.003

Lee, S. S., de Boef Miara, M., Arnold, A. S., Biewener, A. A., & Wakeling, J. M. (2013a). Recruitment of faster motor units is associated with greater rates of fascicle strain and rapid changes in muscle force during locomotion. The Journal of experimental biology, 216(Pt 2), 198–207. https://doi.org/10.1242/jeb.072637

Lee, S. S., Arnold, A. S., Miara, M.deB., Biewener, A. A., & Wakeling, J. M. (2013b). Accuracy of gastrocnemius muscles forces in walking and running goats predicted by one-element and two-element Hill-type models. Journal of biomechanics, 46(13), 2288–2295. https://doi.org/10.1016/j.jbiomech.2013.06.001

Levin, A., & Wyman, J. (1927). The viscous elastic properties of muscle. Proceedings of the Royal Society of London Series B: Biological Sciences, 101 (709), 218-243. doi: 10.1098/rspb.1927.0014

Lichtwark, G. A., & Wilson, A. M. (2005). Effects of series elasticity and activation conditions on muscle power output and efficiency. The Journal of experimental biology, 208(Pt 15), 2845–2853. https://doi.org/10.1242/jeb.01710

Lichtwark, G. A., & Barclay, C. J. (2010). The influence of tendon compliance on muscle power output and efficiency during cyclic contractions. The Journal of experimental biology, 213(5), 707–714. https://doi.org/10.1242/jeb.038026

Loeb, G. E., Hoffer, J. A., & Pratt, C. A. (1985). Activity of spindle afferents from cat anterior thigh muscles. I. Identification and patterns during normal locomotion. Journal of neurophysiology, 54(3), 549–564. https://doi.org/10.1152/jn.1985.54.3.549

Maden-Wilkinson, T. M., Degens, H., Jones, D. A., & McPhee, J. S. (2013). Comparison of MRI and DXA to measure muscle size and age-related atrophy in thigh muscles. Journal of musculoskeletal & neuronal interactions, 13(3), 320–328.

Maganaris CN, Paul JP. In vivo human tendon mechanical properties. J Physiol, 1999; 521 (Pt 1): 307–313.

Magnusson, S. P., Narici, M. V., Maganaris, C. N. & Kjaer, M. Human tendon behaviour and adaptation, in vivo. J. Physiol. 586, 71–81 (2008)

Mann, R. A., & Hagy, J. (1980). Biomechanics of walking, running, and sprinting. The American journal of sports medicine, 8(5), 345–350. https://doi.org/10.1177/036354658000800510

Martin, J. C., & Brown, N. A. (2009). Joint-specific power production and fatigue during maximal cycling. Journal of biomechanics, 42(4), 474–479. https://doi.org/10.1016/j.jbiomech.2008.11.015

Martin, J. C., & Nichols, J. A. (2018). Simulated work loops predict maximal human cycling power. The Journal of experimental biology, 221(Pt 13), jeb180109. https://doi.org/10.1242/jeb.180109

Matson, A., Konow, N., Miller, S., Konow, P. P., & Roberts, T. J. (2012). Tendon material properties vary and are interdependent among turkey hindlimb muscles. The Journal of experimental biology, 215(Pt 20), 3552–3558. https://doi.org/10.1242/jeb.072728

Medler S. (2002). Comparative trends in shortening velocity and force production in skeletal muscles. American journal of physiology. Regulatory, integrative and comparative physiology, 283(2), R368–R378. https://doi.org/10.1152/ajpregu.00689.2001

Meier, P., & Blickhan, R. (2000). FEM-simulation of skeletal muscle: The influence of inertia during activation and deactivation. In W. Herzog (Ed.), Skeletal muscle mechanics: From mechanisms to function (p. 207-233). Chichester, UK: John Wiley & Sons.

Meier U. (2006). A note on the power of Fisher's least significant difference procedure. Pharmaceutical statistics, 5(4), 253–263. https://doi.org/10.1002/pst.210

Meijer K. (2002). History dependence of force production in submaximal stimulated rat medial gastrocnemius muscle. Journal of electromyography and kinesiology : official journal of the International Society of Electrophysiological Kinesiology, 12(6), 463–470. https://doi.org/10.1016/s1050-6411(02)00040-8

Mendez, J., & Keys, A. (1960). Density and composition of mammalian muscle. Metabolism, 9 , 184-188.

Millard, M., Uchida, T., Seth, A., & Delp, S. L. (2013). Flexing computational muscle: modeling and simulation of musculotendon dynamics. Journal of biomechanical engineering, 135(2), 021005. https://doi.org/10.1115/1.4023390

Milner-Brown, H. S., & Stein, R. B. (1975). The relation between the surface electromyogram and muscular force. The Journal of physiology, 246(3), 549–569. https://doi.org/10.1113/jphysiol.1975.sp010904

Monti, R. J., Roy, R. R., Zhong, H., & Edgerton, V. R. (2003). Mechanical properties of rat soleus aponeurosis and tendon during variable recruitment in situ. The Journal of experimental biology, 206(Pt 19), 3437–3445. https://doi.org/10.1242/jeb.00550

Morse, C. I., Degens, H., & Jones, D. A. (2007). The validity of estimating quadriceps volume from single MRI cross-sections in young men. European journal of applied physiology, 100(3), 267–274. https://doi.org/10.1007/s00421-007-0429-4

O'Brien, T. D., Reeves, N. D., Baltzopoulos, V., Jones, D. A., & Maganaris, C. N. (2010). Muscle-tendon structure and dimensions in adults and children. Journal of anatomy, 216(5), 631–642. https://doi.org/10.1111/j.1469-7580.2010.01218.x

Pappas, G. P., Asakawa, D. S., Delp, S. L., Zajac, F. E., & Drace, J. E. (2002). Nonuniform shortening in the biceps brachii during elbow flexion. Journal of applied physiology (Bethesda, Md. : 1985), 92(6), 2381–2389. https://doi.org/10.1152/japplphysiol.00843.2001

Perreault, E. J., Heckman, C. J., & Sandercock, T. G. (2003). Hill muscle model errors during movement are greatest within the physiologically relevant range of motor unit firing rates. Journal of biomechanics, 36(2), 211–218. https://doi.org/10.1016/s0021-9290(02)00332-9

Peterson, C. L., Kautz, S. A., & Neptune, R. R. (2011). Muscle work is increased in pre-swing during hemiparetic walking. Clinical biomechanics (Bristol, Avon), 26(8), 859–866. https://doi.org/10.1016/j.clinbiomech.2011.04.010

Piazza S. J. (2006). Muscle-driven forward dynamic simulations for the study of normal and pathological gait. Journal of neuroengineering and rehabilitation, 3, 5. https://doi.org/10.1186/1743-0003-3-5

Pratt, C. A., & Loeb, G. E. (1991). Functionally complex muscles of the cat hindlimb. I. Patterns of activation across sartorius. Experimental brain research, 85(2), 243–256. https://doi.org/10.1007/BF00229404

Prilutsky B. I. (2000). Coordination of two- and one-joint muscles: functional consequences and implications for motor control. Motor control, 4(1), 1–44. https://doi.org/10.1123/mcj.4.1.1

Rahemi, H., Nigam, N., & Wakeling, J. M. (2014). Regionalizing muscle activity causes changes to the magnitude and direction of the force from whole muscles-a modeling study. Frontiers in physiology, 5, 298. https://doi.org/10.3389/fphys.2014.00298

Rajagopal, A., Dembia, C. L., DeMers, M. S., Delp, D. D., Hicks, J. L., & Delp, S. L. (2016). Full-Body Musculoskeletal Model for Muscle-Driven Simulation of Human Gait. IEEE transactions on bio-medical engineering, 63(10), 2068–2079. https://doi.org/10.1109/TBME.2016.2586891

Roberts, T. J., Marsh, R. L., Weyand, P. G., & Taylor, C. R. (1997). Muscular force in running turkeys: the economy of minimizing work. Science (New York, N.Y.), 275(5303), 1113–1115. https://doi.org/10.1126/science.275.5303.1113

Roots, H., Offer, G. W., & Ranatunga, K. W. (2007). Comparison of the tension responses to ramp shortening and lengthening in intact mammalian muscle fibres: crossbridge and non-crossbridge contributions. Journal of muscle research and cell motility, 28(2-3), 123–139. https://doi.org/10.1007/s10974-007-9110-0

Ross, S. A., & Wakeling, J. M. (2016). Muscle shortening velocity depends on tissue inertia and level of activation during submaximal contractions. Biology letters, 12(6), 20151041. https://doi.org/10.1098/rsbl.2015.1041

Ross, S. A., Nigam, N., & Wakeling, J. M. (2018a). A modelling approach for exploring muscle dynamics during cyclic contractions. PLoS computational biology, 14(4), e1006123. https://doi.org/10.1371/journal.pcbi.1006123

Ross, S. A., Ryan, D. S., Dominguez, S., Nigam, N., & Wakeling, J. M. (2018b). Size, History-Dependent, Activation and Three-Dimensional Effects on the Work and Power Produced During Cyclic Muscle Contractions. Integrative and comparative biology, 58(2), 232–250. https://doi.org/10.1093/icb/icy021

Ross, S. A., Rimkus, B., Konow, N., Biewener, A. A., & Wakeling, J. M. (2020). Added mass in rat plantaris muscle causes a reduction in mechanical work. The Journal of experimental biology, 223(Pt 19), jeb224410. https://doi.org/10.1242/jeb.224410

Ross, S. A., Domínguez, S., Nigam, N., & Wakeling, J. M. (2021). The Energy of Muscle Contraction. III. Kinetic Energy During Cyclic Contractions. Frontiers in physiology, 12, 628819. https://doi.org/10.3389/fphys.2021.628819

Ross, S. A., & Wakeling, J. M. (2021). The energy of muscle contraction. IV. Greater mass of larger muscles decreases contraction efficiency. Journal of the Royal Society, Interface, 18(182), 20210484. https://doi.org/10.1098/rsif.2021.0484

Sawicki, G. S., Robertson, B. D., Azizi, E., & Roberts, T. J. (2015). Timing matters: tuning the mechanics of a muscle-tendon unit by adjusting stimulation phase during cyclic contractions. The Journal of experimental biology, 218(Pt 19), 3150–3159. https://doi.org/10.1242/jeb.121673

Schieber M. H. (1993). Electromyographic evidence of two functional subdivisions in the rhesus monkey's flexor digitorum profundus. Experimental brain research, 95(2), 251–260. https://doi.org/10.1007/BF00229783

Shin, D. D., Hodgson, J. A., Edgerton, V. R., & Sinha, S. (2009). In vivo intramuscular fascicle-aponeuroses dynamics of the human medial gastrocnemius during plantarflexion and dorsiflexion of the foot. Journal of applied physiology (Bethesda, Md. : 1985), 107(4), 1276–1284. https://doi.org/10.1152/japplphysiol.91598.2008

Soman, A., Hedrick, T. L., & Biewener, A. A. (2005). Regional patterns of pectoralis fascicle strain in the pigeon Columba livia during level flight. The Journal of experimental biology, 208(Pt 4), 771–786. https://doi.org/10.1242/jeb.01432

Steele, K. M., Seth, A., Hicks, J. L., Schwartz, M. S., & Delp, S. L. (2010). Muscle contributions to support and progression during single-limb stance in crouch gait. Journal of biomechanics, 43(11), 2099–2105. https://doi.org/10.1016/j.jbiomech.2010.04.003

Syme D. A. (1990). Passive viscoelastic work of isolated rat, Rattus norvegicus, diaphragm muscle. The Journal of physiology, 424, 301–315. https://doi.org/10.1113/jphysiol.1990.sp018068

Thelen D. G. (2003). Adjustment of muscle mechanics model parameters to simulate dynamic contractions in older adults. Journal of biomechanical engineering, 125(1), 70–77. https://doi.org/10.1115/1.1531112

Thelen, D. G., & Anderson, F. C. (2006). Using computed muscle control to generate forward dynamic simulations of human walking from experimental data. Journal of biomechanics, 39(6), 1107–1115. https://doi.org/10.1016/j.jbiomech.2005.02.010

Tijs, C., van Dieën, J. H., & Maas, H. (2015). Effects of epimuscular myofascial force transmission on sarcomere length of passive muscles in the rat hindlimb. Physiological reports, 3(11), e12608. https://doi.org/10.14814/phy2.12608

Uchida, T. K., Seth, A., Pouya, S., Dembia, C. L., Hicks, J. L., & Delp, S. L. (2016). Simulating Ideal Assistive Devices to Reduce the Metabolic Cost of Running. PloS one, 11(9), e0163417. https://doi.org/10.1371/journal.pone.0163417

Van Hooren, B., Teratsias, P., & Hodson-Tole, E. F. (2020). Ultrasound imaging to assess skeletal muscle architecture during movements: A systematic review of methods, reliability, and challenges. Journal of Applied Physiology, 128 (4), 978-999.

van der Made, A. D., Wieldraaijer, T., Kerkhoffs, G. M., Kleipool, R. P., Engebretsen, L., van Dijk, C. N., & Golanó, P. (2015). The hamstring muscle complex. Knee surgery, sports traumatology, arthroscopy : official journal of the ESSKA, 23(7), 2115–2122. https://doi.org/10.1007/s00167-013-2744-0

von Tscharner V. (2000). Intensity analysis in time-frequency space of surface myoelectric signals by wavelets of specified resolution. Journal of electromyography and kinesiology : official journal of the International Society of Electrophysiological Kinesiology, 10(6), 433–445. https://doi.org/10.1016/s1050-6411(00)00030-4

Wang JHC, Guo Q, Li B. (2012). Tendon Biomechanics and Mechanobiology - A Minireview of Basic Concepts and Recent Advancements. Journal of Hand Therapy, 2012; 25(2):133–141.

Wakeling J. M. (2004). Motor units are recruited in a task-dependent fashion during locomotion. The Journal of experimental biology, 207(Pt 22), 3883–3890. https://doi.org/10.1242/jeb.01223

Wakeling J. M. (2009). The recruitment of different compartments within a muscle depends on the mechanics of the movement. Biology letters, 5(1), 30–34. https://doi.org/10.1098/rsbl.2008.0459

Wakeling, J. M., & Horn, T. (2009). Neuromechanics of muscle synergies during cycling. Journal of neurophysiology, 101(2), 843–854. https://doi.org/10.1152/jn.90679.2008

Wakeling, J. M., Lee, S. S., Arnold, A. S., de Boef Miara, M., & Biewener, A. A. (2012). A muscle's force depends on the recruitment patterns of its fibers. Annals of biomedical engineering, 40(8), 1708–1720. https://doi.org/10.1007/s10439-012-0531-6

Wakeling, J. M., Ross, S. A., Ryan, D. S., Bolsterlee, B., Konno, R., Domínguez, S., & Nigam, N. (2020). The Energy of Muscle Contraction. I. Tissue Force and Deformation During Fixed-End Contractions. Frontiers in physiology, 11, 813. https://doi.org/10.3389/fphys.2020.00813

Wakeling, J. M., Tijs, C., Konow, N., & Biewener, A. A. (2021). Modeling muscle function using experimentally determined subject-specific muscle properties. Journal of biomechanics, 117, 110242. https://doi.org/10.1016/j.jbiomech.2021.110242

Walmsley, B., Hodgson, J. A., & Burke, R. E. (1978). Forces produced by medial gastrocnemius and soleus muscles during locomotion in freely moving cats. Journal of neurophysiology, 41(5), 1203–1216. https://doi.org/10.1152/jn.1978.41.5.1203

Zajac F. E. (1989). Muscle and tendon: properties, models, scaling, and application to biomechanics and motor control. Critical reviews in biomedical engineering, 17(4), 359–411.

Zajac, F. E., & Gordon, M. E. (1989). Determining muscle's force and action in multi-articular movement. Exercise and sport sciences reviews, 17, 187–230.

Zurlo, F., Larson, K., Bogardus, C., & Ravussin, E. (1990). Skeletal muscle metabolism is a major determinant of resting energy expenditure. The Journal of clinical investigation, 86(5), 1423–1427. https://doi.org/10.1172/JCI114857